catalysts

MDPI

Article

Iron Promoted TiO_2-Activated Carbon Nanocomposites for Photocatalytic Degradation of Congo Red in Water

Daniela Negoescu [1], Veronica Bratan [1,*], Mihaela Gherendi [2], Irina Atkinson [1], Daniela C. Culita [1], Andreea Neacsu [1], Adriana Baran [1], Simona Petrescu [1] and Viorica Parvulescu [1,*]

[1] Institute of Physical Chemistry "Ilie Murgulescu", Romanian Academy, 060021 Bucharest, Romania; danielan@icf.ro (D.N.); iatkinson@icf.ro (I.A.); dculita@icf.ro (D.C.C.); neacsudanaandreea@yahoo.com (A.N.); abaran@icf.ro (A.B.); simon_pet@yahoo.com (S.P.)

[2] National Institute for Lasers, Plasma and Radiation Physics, 077125 Magurele-Ilfov, Romania; mihaela.gherendi@inflpr.ro

* Correspondence: vbratan@icf.ro (V.B.); vpirvulescu@icf.ro (V.P.)

Abstract: Nanocomposites containingTiO_2 and activated carbon were obtained by the sol-gel method in the presence of Brij 58 surfactant. The sample with a higher surface area (185.6 m^2/g) was promoted with Fe by impregnating it with aqueous solution of $Fe(NO_3)_3$. The obtained iron loadings, measured using X-ray fluorescence, were 0.83%, 3.30% and 7.17%. TiO_2 anatase was identified in all the samples by X-ray diffraction and Raman spectroscopy, but the presence of iron oxides could not be detected. However, infrared spectroscopy indicated the existence of Fe-O and Fe-O-Ti bonds. X-ray photoelectron spectroscopy revealed the presence of Fe^{2+} for samples with a lower Fe content and a mixture of Fe^{2+} and Fe^{3+} in the sample with 7.17% Fe. UV-Vis and photoluminescence spectroscopy showed the presence of carbon and Fe alongside TiO_2. This combination led to new properties due to the generation of intermediate energy levels and defects, contributing to an enhancement in the photocatalytic performance. The highest photodegradation efficiency of Congo red in solution (84.46%) was obtained for the sample with 7.17% Fe under visible light irradiation and acidic conditions. The synergistic contribution of dye adsorption and photodegradation was demonstrated, taking into account ZPC values of nanocomposites. Kinetic studies were completed with reaction mechanisms based on the results obtained in the presence of scavengers.

Keywords: Fe/TiO_2-activated carbon; nanocomposites; photocatalysts; photodegradation; textile dyes; Congo red

check for updates

Citation: Negoescu, D.; Bratan, V.; Gherendi, M.; Atkinson, I.; Culita, D.C.; Neacsu, A.; Baran, A.; Petrescu, S.; Parvulescu, V. Iron Promoted TiO_2-Activated Carbon Nanocomposites for Photocatalytic Degradation of Congo Red in Water. *Catalysts* **2024**, *14*, 844. https://doi.org/10.3390/catal14120844

Academic Editor: Fei Chang

Received: 4 October 2024
Revised: 15 November 2024
Accepted: 19 November 2024
Published: 22 November 2024

Copyright: © 2024 by the authors. Licensee MDPI, Basel, Switzerland. This article is an open access article distributed under the terms and conditions of the Creative Commons Attribution (CC BY) license (https://creativecommons.org/licenses/by/4.0/).

1. Introduction

Dyes represent an important category of harmful chemical substances found in wastewater [1–4]. However, the most polluting industry is the textile one, with more than 10,000 types of synthetic dyes used [4]. Each year, approximately 280,000 tons of textile dyes are spilled into water sources worldwide [5]. When it comes to the impact on health, dyes can cause several medical conditions, such as skin, respiratory or gastrointestinal diseases. They can also have carcinogenic and mutagenic effects [2,3,6–10]. Additionally, dyes can have a negative impact on the aquatic environment, because sunlight can no longer penetrate the water as easily [10,11]. This effect is more pronounced due to the fact that these compounds have a stable aromatic molecular structure and are very soluble in water. Congo red (CR) is one of the dyes frequently used in the textile industry, with a potential mutagenic and mitotic effect. Its structure consists of benzene and naphthalene rings that are difficult to degrade [12]. Hence, it is necessary to find effective methods for degradation of the dissolved dyes in water. The most used methods are (i) physicochemical processes such as adsorption, coagulation or membrane filtration; (ii) biological (using bacteria, algae or enzymes) and (iii) chemical, also known under the name of "advanced oxidation processes" (AOPs) [2,3,8,13]. AOPs are highly efficient because they lead to the

rapid and non-selective degradation of various organic pollutants in water [6,14–18]. The photocatalysis, as an AOPs, uses a semiconductor (photocatalyst) to generate an electron-hole pair under light irradiation. These particles react with water and oxygen molecules, resulting in radicals with oxidizing properties (such as hydroxyl •OH and superoxide anion $\bullet O_2^-$ radicals) that can break the chemical bonds in the organic molecules.

TiO_2 is a well-known semiconductor used as a photocatalyst because of its chemical stability, high activity, and low production cost [15,18–22]. However, it also presents several disadvantages (low surface area, weak adsorption capacity, and wide band gap) that limit its use in photocatalytic reactions. A large band gap implies that higher light energy is required for the electrons to pass from the valence band (VB) to the conduction band (CB) [23,24]. Various methods have been used to extend the application of TiO_2 in the visible range.

The two most common methods are non-metallic and metallic doping [25–34]. Thus, carbon can be used either as a non-metallic dopant for TiO_2 or as an additional component in composite materials [35,36]. However, activated carbon (AC) is reportedly very effective in water purification by adsorption [37], thanks to its large surface area and porosity. Both AC and some metal components of the composites with photocatalytic activity were obtained by green synthesis using plant extracts or carbonaceous waste [15,38–41]. Incorporating metal oxide semiconductors, with a cost-friendly carbon phase, is a promising strategy for eliminating hazardous organic pollutants [41]. AC facilitates the transfer of charge carriers in the nanocomposites and prevents their recombination. The addition of AC in TiO_2 extends the light absorption of the final material to the visible range and enhances its specific surface area. It has been reported that the synergistic effect of single-electron-trapped oxygen vacancies and carbon species is responsible for the improved photodegradation efficiency of the carbon-TiO_2 heterostructures in visible light [42–44]. Various synthesis methods, including mechanical mixing [9,10], sol-gel [14,15], hydrothermal [11], and microwave techniques [24], have been used to obtain TiO_2-AC photocatalysts.

On the other hand, the transitional metal ions incorporated into the titania lattice can reduce its band gap and extend the light absorption in the visible range. Additionally, metallic ions can act as electron or hole traps, facilitating their separation [45,46]. In this regard, iron is a promising choice because it is non-toxic and affordable, being the second most abundant metal on Earth [47]. The interaction between iron oxide, with different stoichiometric structures, and TiO_2 results in a narrower band gap [48–50]. Iron also weakens the adjacent Ti-O bonds, leading to the formation of oxygen vacancies. Their presence promotes water and/or oxygen adsorption onto the photocatalyst surface by generating reactive oxygen species (ROS). As a result, Fe-doped samples exhibit improved photocatalytic activity compared to pure TiO_2 [50–52]. Another method to obtain an effective charge separation is to create iron oxide nanoparticles-AC-TiO_2 heterojunctions [35,48,51–53]. Composite photocatalysts obtained by mixing a carbon compound (graphitic carbon nitride g-C_3N_4, graphene, or reduced graphene oxide) with TiO_2 and a metal oxide, such as Fe_3O_4, were applied in the photocatalytic removal of textile dyes [35,48,52–54].

In this study, TiO_2-AC composites were prepared using the sol-gel method in the presence of a surfactant (Brij58). The amount of AC (obtained from coffee grounds activated with H_3PO_4) was varied to follow its effect on the properties of the resulting materials. The TiO_2-AC sample with a higher P concentration (1.33%) was used as support for Fe oxides in varying amounts. The materials were then analyzed for morphology, crystalline structure, texture, composition, and optical properties. Subsequently, the samples were tested for their effectiveness in the photocatalytic degradation of Congo red dye in water. Additionally, the effect of the composition of the obtained materials on their photocatalytic properties, the selectivity to water mineralization, kinetics and the reaction mechanism was also evaluated. The degree of novelty of this study is given both by the synthesis method used and by the characteristics of the resulting composite materials, especially considering the fact that similar systems were studied in a limited extent in the photodegradation of Congo red dye.

2. Results

2.1. Characterization of the Photocatalysts

Previous studies [15,55–57] have shown that AC can be used to synthesize TiO_2-based composites with photocatalytic properties, and it was demonstrated that the conditions of carbon activation have a major influence on the properties of the obtained composites [15]. Herein, coffee grounds were pretreated with orthophosphoric acid solution and then washed with hot distilled water using various water/solid mass ratios. Two activated carbon samples, referred to as AC0 and AC, resulted. These samples were used as co-surfactants alongside Brij 58 in the sol-gel synthesis of TiO_2. Consequently, one sample (TiO_2AC0) was obtained with AC0, and two more samples (TiO_2AC1, and TiO_2AC2) were prepared using AC (with Ti alkoxide/AC mass ratio of 14 and 16, respectively). The TiO_2AC1 sample, which exhibited a larger surface area (Table 1), was impregnated with an aqueous solution of iron nitrate. The concentration of the solution was calculated to obtain three samples with 1 wt.%, 5 wt.% and 10 wt.% Fe_2O_3, labeled Fe1-TiO_2AC1, Fe5-TiO_2AC1, and Fe10-TiO_2AC1.

Table 1. Structural, textural and optical properties of the prepared samples.

Sample	D_A [1] (nm)	S_{BET} [2] (m^2/g)	V_p [3] (nm^3)	D_p [4] (nm)	E_g [5] (eV)
TiO_2AC0	10.7	82.2	0.21	7.6	3.24
TiO_2AC1	8.4	185.6	0.34	9.0	3.36
TiO_2AC2	7.5	157.2	0.33	9.4	3.34
Fe1-TiO_2AC1	5.1	101.4	0.33	11.96	3.29
Fe5-TiO_2AC1	6.0	95.8	0.31	11.64	3.08
Fe10-TiO_2AC1	5.7	88.8	0.27	11.11	2.87

[1] D_A-anatase crystallite diameter; [2] S_{BET}-specific surface area; [3] V_p-volume of the pores; [4] d_p-pore diameter; [5] E_g-band gap energy calculated from direct transitions.

2.1.1. Crystalline Structure, Morphology, Texture and Composition

The X-ray diffractograms for TiO_2AC0, TiO_2AC1, and TiO_2AC2 are presented in Figure 1a. The formation of anatase as the single crystalline phase for all samples can be attributed to the lower calcination temperature (450 °C) and/or the AC presence in the synthesis medium. It was previously observed that AC can inhibit the conversion to rutile even when calcination takes place at higher temperatures [58,59]. The reduced intensity of the diffraction peaks obtained for the TiO_2AC samples may be due to the shielding effect of carbon during the sol-gel process [60]. As shown in Figure 2a, the (101) peak of the samples TiO_2AC1 and TiO_2AC2 is slightly shifted to lower values of 2θ (25.4° and 25.5°, respectively) compared to TiO_2AC0 (25.6°), suggesting stronger interaction of carbon with TiO_2 for these two samples. Ti-C bonds (longer than Ti-O) are probably formed. Additionally, because the carbon atom is larger than oxygen, an expansion of the TiO_2 lattice results [61].

The average size of the crystallite, determined from Scherrer's equation considering the (101) peak, is presented in Table 1 as "D_A". These values decrease as the amount of AC increases. This is probably the effect of the carbon particles present in the synthesis mixture that act as boundaries and inhibit the growth of TiO_2 crystallites.

The X-ray diffractograms of the Fex-TiO_2AC1 samples (where x = 1, 5, 10) are depicted in Figure 1b. They show broad Bragg peaks, suggesting the formation of small-sized particles or poorly crystallized materials. The identified reflections belong to the anatase. The absence of diffraction lines characteristic of iron oxides may be due to the good dispersion of the iron oxide phase, the formation of an amorphous phase or of the Ti-O-Fe bonds on the surface. It is also highly likely that the substitution of Ti^{4+} by Fe^{3+} ions occurred due to their similar ionic radii (0.68 A for Ti^{4+} vs. 0.64 A for Fe^{3+}) [62,63].

Moreover, the presence of carbon in the composite material used as a support can significantly promote the formation of the amorphous phase of iron oxide (most pronounced in the Fe10-TiO_2AC sample) [63].

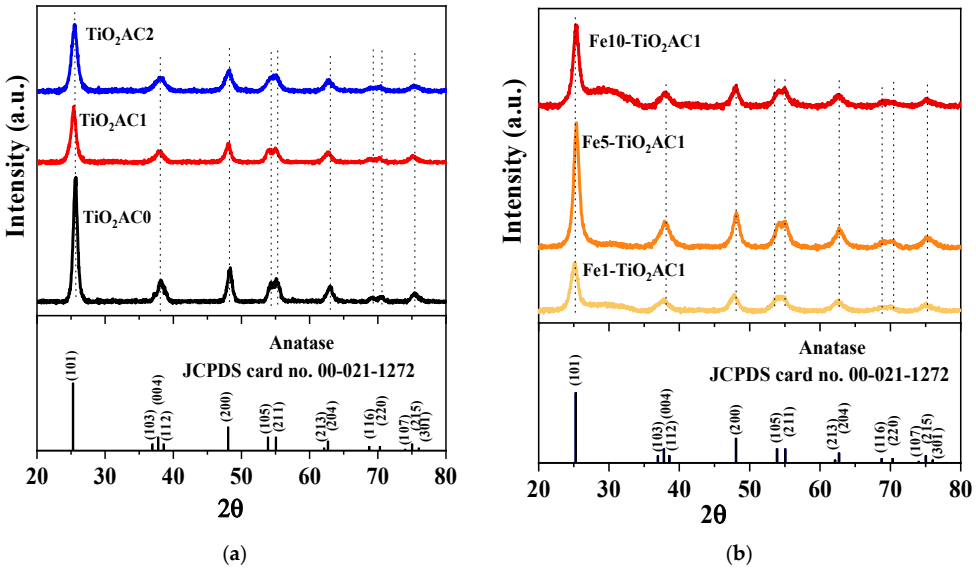


Figure 1. XRD patterns of the (**a**) TiO_2AC and (**b**) Fex-TiO_2AC1 samples.

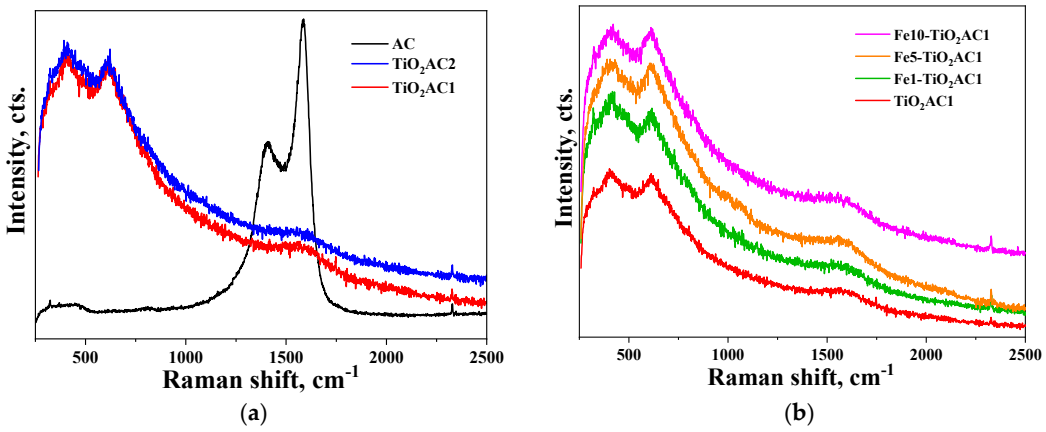
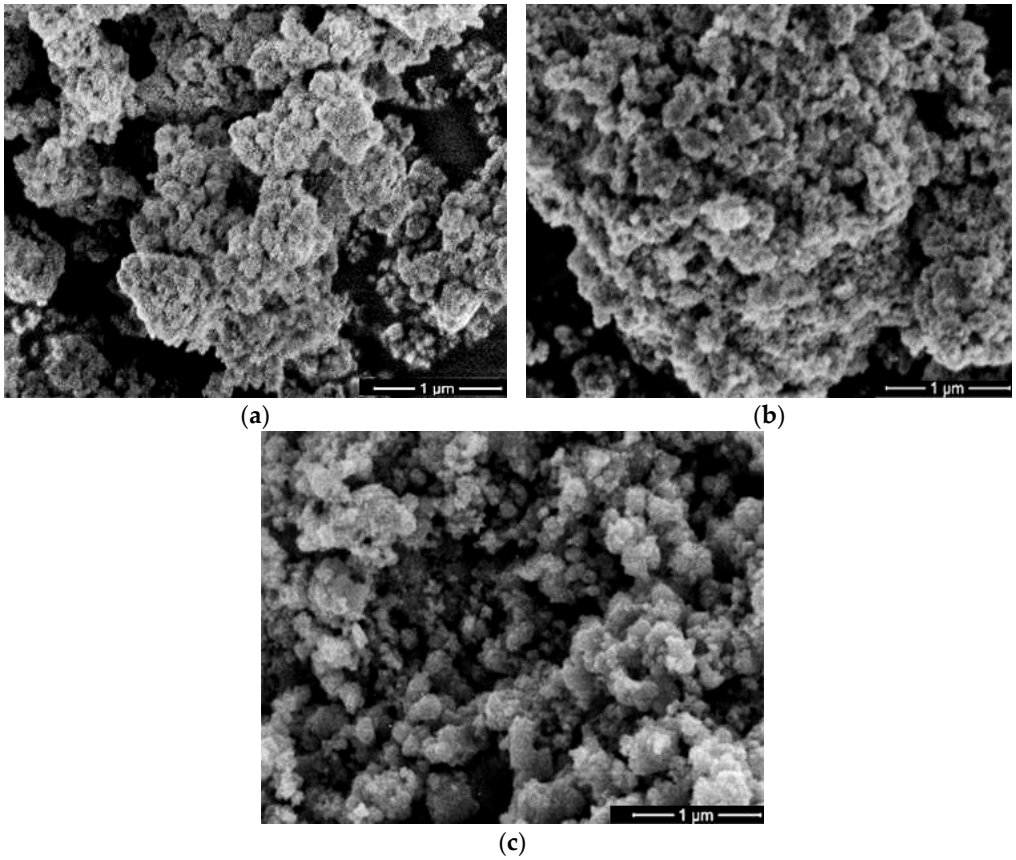


Figure 2. Raman spectra of (**a**) the AC and TiO_2AC nanocomposites, and (**b**) the samples that contain iron oxide.

UV-Raman spectroscopy enables accurate detection of the phase composition in the surface region. Figure 2a illustrates the Raman spectra of the obtained AC and TiO_2-AC composite samples. The AC sample exhibits two notable bands: the D band, also known as the disorder band (A_{1g} mode), at 1407 cm^{-1} and the G band (E_{2g} mode of in-plane vibration of the C-C bond) at 1585 cm^{-1}. These bands are attributed to sp^2 hybridized carbon [64]. In the AC-TiO_2 composite samples, the TiO_2 structure is revealed by Raman bands that correspond to the active modes of the anatase phase at 400 (B_{1g}), 500 (A_{1g}) and 631 (E_g symmetry) cm^{-1} [65]. Notably, the characteristic bands of the AC appear in all spectra. Regarding the impregnated Fe samples (Figure 2b), both TiO_2 and AC are strong scatters, unlike iron oxides (except hematite), which are weak scatters, masking their Raman bands. Additionally, the Raman bands of α-Fe_2O_3 overlap with those of TiO_2. Therefore, a clear indication of the presence of iron oxides cannot be detected in the Raman spectra of the materials under discussion. However, the shoulder at about 500 cm^{-1} in anatase vanished when the iron oxide content increased up to 10% [66].

The morphology of the synthesized samples was examined using scanning electron microscopy (SEM). The obtained micrographs (Figure 3) display clusters of nanoparticles with a spherical shape for all Fe-TiO_2AC1 samples. These samples preserve the morphology of the TiO_2AC1 support (Figure S1). Based on the average crystallite sizes (Table 1) obtained from XRD and on the SEM images, it can be inferred that the particles in the Fe-TiO_2AC1 samples are polycrystalline or may consist of small crystalline nanoparticles with a strong tendency to agglomerate.



(**a**) (**b**) (**c**)

Figure 3. SEM images of the Fe1-TiO_2AC1 (**a**), Fe5-TiO_2AC1 (**b**), and Fe10-TiO_2AC1 (**c**) samples, respectively.

The N_2 adsorption-desorption experiments revealed type IV isotherms for all the samples (Figure 4). The TiO_2AC1, TiO_2AC2, and Fex-TiO_2AC1 nanocomposites exhibited a H3 hysteresis loop, while TiO_2AC0, which has a lower carbon content and no P (Table 2), displays a H2-type hysteresis. It is evident from Figure 4 that the properties and amount of AC (inserted figures) have a higher influence on the isotherms and pores size distribution than the iron loading. Therefore, TiO_2 with a lower carbon content has a wider pore size distribution. Furthermore, increasing the amount of AC results in increasing the BET surface area and pore volume (Table 1). The highest values were obtained for the TiO_2AC1 sample.

The composition of the samples was determined using X-ray fluorescence. The results, expressed as weight %, are listed in Table 2. The XRF analysis confirmed that carbon and iron were successfully immobilized in the samples. Additionally, phosphorus was detected in all materials, except TiO_2AC0, from the carbon activation procedure (with phosphoric acid). As expected, the TiO_2AC2 sample had the highest carbon content.

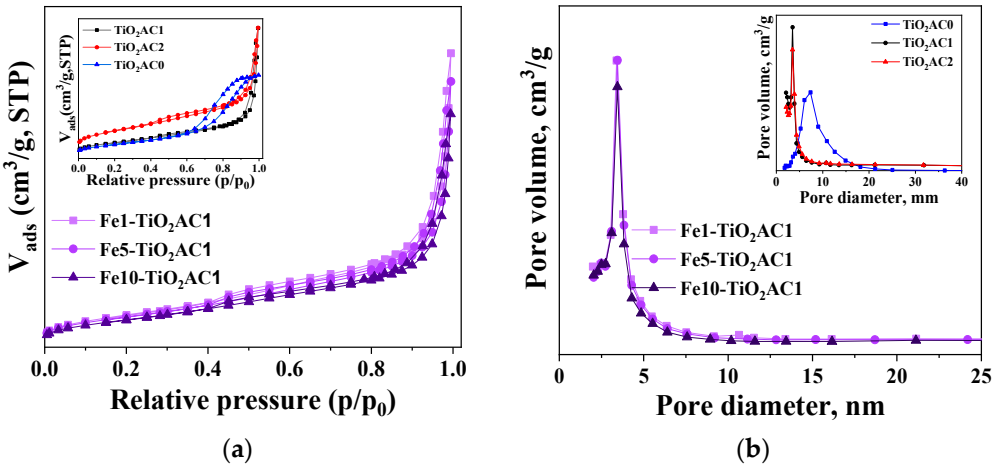


Figure 4. Nitrogen adsorption-desorption isotherms (**a**) and pore size distribution (**b**) of the TiO_2AC and Fex-TiO_2AC1 samples.

Table 2. Elemental composition of the prepared samples, expressed as wt.%, as resulted from XRF.

Sample	Ti	O	Fe	C	P
TiO_2AC0	58.56	39.84	-	1.60	-
TiO_2AC1	55.62	40.65	-	2.40	1.33
TiO_2AC2	54.80	40.63	-	3.62	0.95
Fe1-TiO_2AC1	56.55	39.71	0.83	1.88	1.03
Fe5-TiO_2AC1	53.97	40.05	3.30	1.73	0.95
Fe10-TiO_2AC1	50.88	39.29	7.17	1.82	0.84

When comparing the results obtained from XRF (Table 2) with those from XPS (Table 3), a significant difference in the elemental composition between the surface and the bulk material can be noticed. Specifically, the percentages of surface titanium and oxygen are lower, while the carbon, phosphorus and iron contents are higher on the surface than in the volume. Additionally, the decrease in surface titanium content aligns with the increase in carbon amount used in the synthesis process. Among the Fe-doped samples, Fe1-TiO_2AC exhibits the lowest concentration of titanium ions and the highest concentration of iron on the surface. This suggests that, at lower concentrations, most of the iron remains at the surface, either bound to titanium ions and forming Ti-O-Fe bonds or creating small deposits of amorphous oxides. At higher concentrations, the iron disperses more throughout the material, particularly within the channels of the support volume, where it can interact with TiO_2 or form iron oxide nanoparticles on the pore surfaces. These findings are supported by XRD (Figure 1b), which indicates a dominant anatase phase for the Fe-doped samples and the appearance of a small percentage of the amorphous phase, probably iron oxide. Table 3 also shows that Fe5-TiO_2AC has the lowest amount of Fe and the highest amount of carbon on the surface among the Fe-containing samples, suggesting better iron dispersion in this case.

In the high-resolution XPS spectra of Ti2p for the samples TiO_2AC0, TiO_2AC1, and TiO_2AC2 (Figure S2), two symmetric peaks can be identified: Ti-$2p_{3/2}$ at approximately 458 eV and Ti-$2p_{1/2}$ at around 463.5 eV. These peaks are attributed to Ti^{4+} in TiO_2 [15,67]. The separation between the two Ti^{4+} peaks is 5.7 eV, which agrees with the theoretical difference and confirms the existence of the TiO_2 compound [68]. However, slight variations in the binding energy (BE) values are observed with the increasing carbon content. Thus, the BE of the core Ti-$2p_{3/2}$ peaks decreases by 0.1 for TiO_2AC2 and 0.5 eV for TiO_2AC1. This shift may be due to the modification of the coordination sphere of the Ti^{4+} ions, resulting

from the incorporation of carbon in the TiO_2 lattice, as also indicated by the XRD data. In the case of the Fe-containing samples, both Ti-$2p_{3/2}$ and Ti-$2p_{1/2}$ envelopes contained a contribution from three peaks, with slightly varying weights from sample to sample (Figure S3). A single, relatively large peak, included to fill the envelope on the high-energy side, is associated with surface structures. The main peak (458.8 eV–458.9 eV) is assigned to the TiO_2 anatase phase, while the peak in the low energy side of the envelope corresponds to the suboxide TiO_{2-x} phase. This may suggest the dispersion of Fe^{3+} ions within the TiO_2 framework and a charge transfer from the Ti^{4+} to Fe^{3+} ions, leading to the formation of Fe^{2+} species and the Ti-O-Fe structure [63], in accordance with the XRD and Raman results. For the Fe10-TiO_2AC1 sample, an additional peak had to be introduced in the high energy side of both $2p_{3/2}$ and $2p_{1/2}$ envelopes (at 460.5 eV and 466.4 eV). The shift towards a higher BE than those of TiO_2 indicates a change in the electronic environment of Ti after iron oxide immobilization [45]. The chemical environment of Ti^{4+} is different in this case, though the oxidation number is the same.

Table 3. XPS data for the photocatalysts (composition of the chemical species expressed in wt.%).

Sample	Ti	O	Fe	C	P
TiO_2AC0	51.88	39.34	-	8.78	-
TiO_2AC1	47.37	43.65	-	8.98	-
TiO_2AC2	43.41	44.66	-	7.63	4.30
Fe1-TiO_2AC1	43.70	36.69	14.47	3.36	1.78
Fe5-TiO_2AC1	46.88	37.77	6.83	6.76	1.76
Fe10-TiO_2AC1	47.01	37.90	8.16	5.13	1.80

The presence of suboxide compounds of titanium or iron is confirmed by the complex structure of the O1s spectral line, which results from the convolution of three peaks (Figures S4 and S5). The peak around 529.5 eV and the one at around 530.5 eV correspond to the Ti-O and C-O bonds, respectively [68]. The higher amount of AC during synthesis causes a shift to lower energies of the Ti-O bond. Hence, for TiO_2AC1, the peak has a maximum at 529.0 eV and, for TiO_2AC2, at 529.4 eV. Carbon can be incorporated into a TiO_2 lattice by substituting the O site and forming an O-Ti-C bond and changing the binding energy. The most significant shift is observed for the TiO_2AC1 sample and may be related to more carbon inserted into the TiO_2 lattice. Furthermore, the appearance of another peak at 530.6 eV for TiO_2AC2 is attributed to the -OH bond on the surface [69–71]. For the Fe-containing samples, the convolution of the XPS spectra reveals three peaks assigned to the Ti-O, Fe-O and C-O bonds, respectively, with different contributions. In both cases, the O1s core level is centered around 530 eV, which corresponds to the binding energy of the metal oxide (TiO_2). A shoulder is noted at around 533 eV, associated with the OH groups on the surface.

In addition to titanium and oxygen, a carbon peak was also detected for all prepared samples. The convoluted 1s spectra (Figures S6 and S7) show two peaks at 284.2 and 287.2 eV for the TiO_2AC0 sample, while, for the TiO_2AC1 and TiO_2AC2 samples, there are three peaks located at 283.4/283.9, 284.7/285.4 and 287.4/287.5 eV. The first peak at ~283.5 eV corresponds to sp^2 graphitic carbon, which is usually found on the surface of the samples (also known as adventitious carbon). The second peak is assigned to the C-C bond, and the last peak indicates the presence of C-O bonds, particularly Ti-O-C [15,71]. The same peaks appear in the spectra of the Fe-containing samples. The P2p spectra (Figure S8) of the Fex-TiO_2AC1 samples were fitted with two peaks at 134.2 eV and 133.2 eV attributed to the P-O and P-C species [15]. In conclusion, these samples contain phosphorus (P^{5+}) with four oxygen neighbors (PO_4 groups) and C-P bonds as a result of the successful activation of carbon.

The Fe $2p_{3/2}$ envelopes were well-fitted using the multiplets described by Gupta and Sen [72,73] as a starting point for analyzing high-spin Fe^{3+} and Fe^{2+} compounds (Figure 5). Except for Fe10-TiO_2AC1, all iron-containing samples exhibited a Fe $2p_{3/2}$ structure. This structure consists of a low-intensity peak on the lower binding energy side of the envelope, followed by a peak associated with the presence of metallic Fe(0) [74]. The formation of reduced iron species can be the result of its strong interaction with TiO_2 support (SMSI) [75], facilitated, in this case, by the presence of carbon in the thermal treatment. The main part of the structure is formed by Fe^{2+} $2p_{3/2}$ multiplets corresponding to the FeO phase [73,76]. To fully describe the entire envelope, a peak associated with the surface structures was also introduced at the higher binding energy side. The Fe $2p_{3/2}$ envelope is larger and richer in the case of the Fe10-TiO_2AC1 sample. The Fe^{2+} multiplets remain the most intense, while the higher binding energy side of the structure is well-fitted by introducing the Fe^{3+} multiplets. Their presence indicates the formation of the Fe_2O_3 phase.

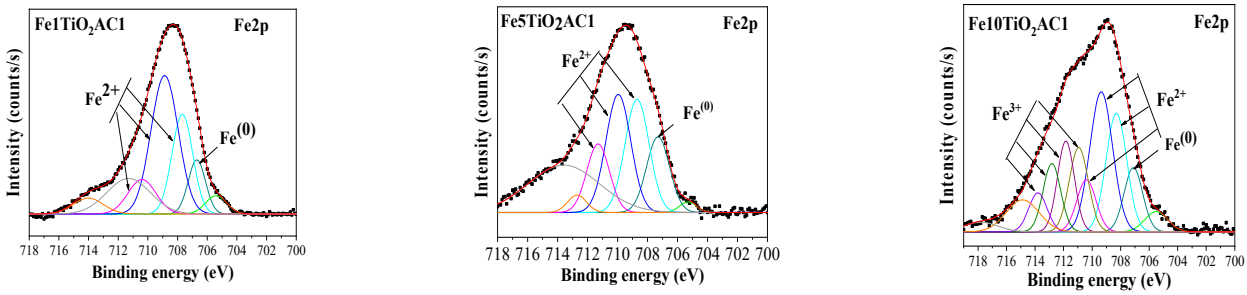


Figure 5. High-resolution Fe2p XPS spectra for the Fex-TiO_2AC (were x = 1, 5, 10) samples.

The vibrational spectra of the TiO_2AC1, Fe1-TiO_2AC1, Fe5-TiO_2AC1, and Fe10-TiO_2AC1 samples were recorded between 400 and 4000 cm^{-1}, as shown in Figure 6a. Usually, the absorption features at 460 cm^{-1}, 760 cm^{-1}, and 560 cm^{-1} are characteristic of the Ti-O bond, anatase phase and $\nu_{Ti\text{-}O}$ of condensed octahedral (TiO_6), respectively, while Fe-O shows an asymmetric vibration at 760 cm^{-1} and an absorption peak at 560 cm^{-1} due to the Fe-O stretching mode [62,77]. Thus, the broadband that appears for all the samples between 400 and 900 cm^{-1} can be assigned to the presence of the TiO_2 and iron oxide species. Since its intensity decreases as the iron concentration increases, it can be inferred that the absorption primarily originates from TiO_2 contributions.

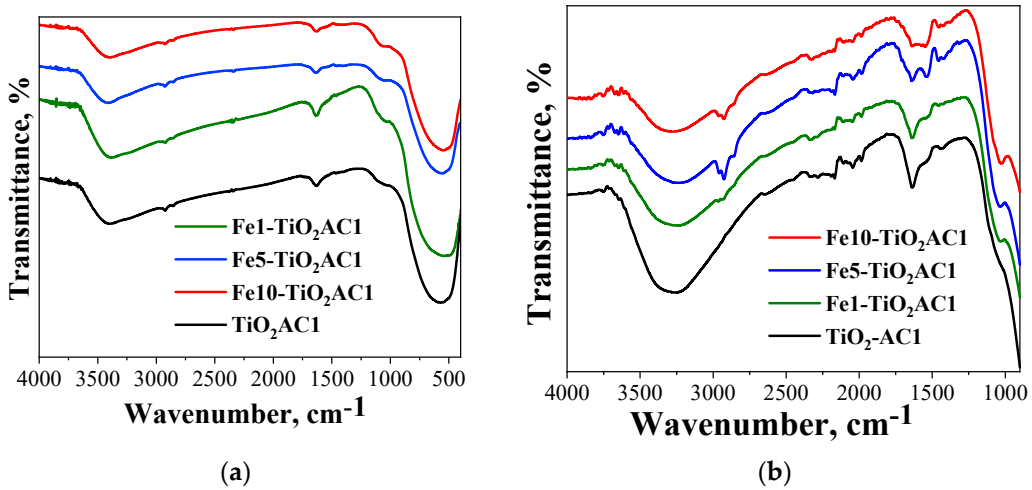


Figure 6. FTIR (**a**) and ATR-FTIR (**b**) spectra of the nanocomposites.

The recorded ATR-FTIR spectra of nanocomposites are also presented in Figure 6b. The band centered at around 3250 cm^{-1} can be related to the superposition of the vibration

band of the hydroxyl group and the stretching vibration of the adsorbed water molecule. As the amount of Fe increases, the band maximum shifts towards higher frequencies. This shift may be attributed to stronger hydrogen bonding interactions that occur upon the formation of the nanocomposites. The peaks observed at 2960 cm^{-1} and 2925 cm^{-1} are mainly due to the stretching vibration of the C=O bond. The bands between 2500 and 2300 cm^{-1} correspond to the stretching of C-O bonds and the peak at 1643 cm^{-1} is associated with the stretching and bending vibrations of the -OH groups. These functional groups are believed to influence phase formation and stabilization in all the nanocomposites [77]. In the Fex-TiO_2AC1 samples, the peaks at 1454 cm^{-1} and 1423 cm^{-1} are assigned to the vibration of the TiO_2 lattice in the presence of AC and Fe. All Fex-TiO_2AC samples display increased absorption around 1034 cm^{-1}, which is attributed to the Fe-O-Ti stretching vibrations [78,79]. Although this band is very low in intensity, its amplitude increases in line with the iron concentration in the nanocomposites.

2.1.2. Optical Properties

The optical properties of the photocatalysts were investigated using UV-Vis and photoluminescence spectroscopy. DR UV-Vis spectroscopy is a simple technique for determining the band gap values of the materials because it permits the direct measurement of powder samples. From the recorded spectra (Figure 7), it is observed that all three TiO_2AC samples show strong absorption in the UV range, which is ascribed to the characteristic electronic transitions from the VB to the CB in TiO_2. However, the incorporation of carbon into the titania results in extended light absorption at wavelengths higher than 400 nm, which can be attributed to the absorption of free carriers or deep electronic levels related to the carbon presence [71]. The UV-Vis spectra for the Fex-TiO_2AC1 samples also exhibit the characteristic peak related to inter-band transitions in TiO_2. A shift in light absorption towards longer wavelengths, which increases with the Fe content, is noticeable in the spectra of Fe-doped samples. For the Fe10-TiO_2AC1 sample, a small peak appears at 500 nm, assigned to the pair excitation process ($^6A_1 + {}^6A_1 \rightarrow {}^4T_1 + {}^4T_1$) between two adjacent Fe^{3+} cations [76,80]. However, the absorption in the visible region due to the carbon incorporation is no longer visible. This could be due to the screening effect, as the iron oxides were impregnated onto the surface of the TiO_2-AC1 composite. Another potential reason lies in the synthesis procedure, which includes an additional calcination step when the surface carbon can be oxidized.

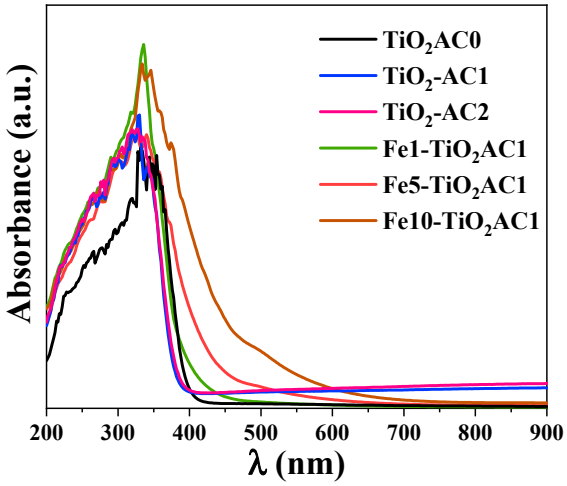


Figure 7. UV-Vis absorption spectra of the nanocomposites.

The band gap energies (E_g) were determined from Tauc plots (Figure S9a), and the obtained values are included in Table 1. To compare all the samples, including those with iron, the E_g was calculated supposing direct transitions. The obtained values for the C-doped samples increase with the increasing carbon amount. Most published articles

report a narrowing of the TiO_2 band gap after carbon addition [15,42,60,61,68,81], while only few exceptions notice its widening [58,82]. Furthermore, the high carbon amount in the samples, larger than the typical dopant concentration of 0.5–2 wt.%, can be another explanation [44]. The increase in the dopant concentrations leads to the occupation of the electronic levels existing in CB and produces an increase in the optical band gap (the Moss-Burstein effect) [58]. The E_g values of the Fe-TiO_2 samples (Table 1) decrease from 3.29 eV (for the Fe1-TiO_2AC1 sample) to 2.87 eV (for Fe10-TiO_2AC1) as the iron content increases. However, it is well known that anatase has an indirect band gap of 3.2 eV. To highlight the effect of carbon on anatase, E_g was also calculated from indirect transitions for the TiO_2AC0 sample. The obtained value was 2.94 eV (Figure S9b).

The photoluminescence (PL) spectra of the synthesized materials (Figure 8) display two emission peaks. The main peak, located around 425 nm, is attributed to the radiative recombination of photogenerated electrons from the CB with holes in the VB. The peak near 500 nm is likely related to the combination of trapped electrons from oxygen vacancies and surface defects induced by the AC and Fe presence [54]. The highest intensity of the peaks is obtained in the case of TiO_2AC0, which is related to the quick recombination of the photogenerated charge carriers, and the formation of more defects, such as surface oxygen vacancies, respectively. Among the Fe-modified samples, Fe5-TiO_2AC1 exhibits the highest intensity. This observation may confirm the possible substitution of the iron ions in the TiO_2 network [33], which correlates well with the result of the previous characterizations.

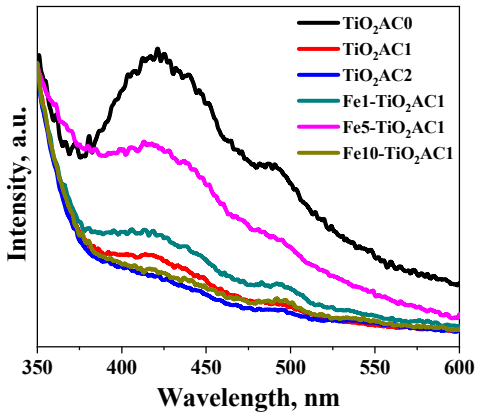


Figure 8. PL spectra of the obtained nanocomposite materials.

2.2. Photocatalytic Properties of the Nanocomposite Materials

2.2.1. Congo Red Removal by Adsorption and Photocatalytic Reactions

The potential use of the nanocomposites obtained was explored in the photodegradation of CR, an amino benzidine-based diazo dye (Figure S10). The photocatalytic properties of the nanocomposite materials were evaluated both before and after the immobilization of iron. The photodegradation of CR dye was monitored over time by measuring the decrease in absorbance of the characteristic peak at 498 nm. Only 16.8% of CR dye degradation was observed after 300 min without a photocatalyst. Previous experiments were conducted to determine the time needed to establish adsorption-desorption equilibrium, and it was found that 30 min is sufficient for this purpose (Figure S11).

Figure 9 displays the results of the CR photodegradation in the presence of TiO_2ACn (Figure 9a) and Fex-TiO_2AC1 (Figure 9b) as photocatalysts. The experiments were conducted at pH = 6, characteristic of the reaction medium. All samples, except for TiO_2AC1 and TiO_2AC2, demonstrate high efficiency in removing CR (Figure 9). For the Fe10-TiO_2AC1 sample, the reaction was also carried out under acidic conditions (pH = 2), yielding the best results. Decreasing the pH of the solution from 6 to 2 increases the removal efficiency of CR from 67% to 85%. This enhanced activity at a lower pH is attributed to the anionic nature of the CR dye, which contains two sulfonic groups that readily ionize in acidic conditions, forming a soluble CR anion. The measurements of

the point of zero charge (PZC) values and the corresponding pH levels are also presented in Figure S12 and Table 4. Therefore, in acidic pH conditions, positively charged species are present on the surface of the photocatalysts, which favors the adsorption of dye anions and enhances the photocatalytic reaction.

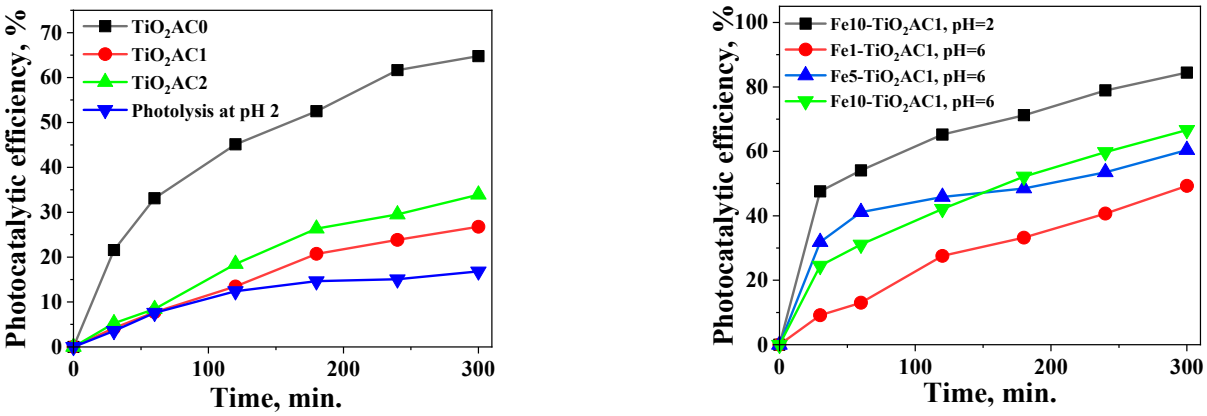


Figure 9. The efficiency of CR removal without the catalyst, and in the presence of TiO_2AC (**a**) and Fex-TiO_2AC photocatalysts (**b**) under visible irradiation and pH = 6, except Fe10-TiO_2AC1, for which the reaction was also carried out at pH = 2.

Table 4. Point of zero charge (PZC) values and of the corresponding pH.

Sample	TiO_2-AC1	Fe1-TiO_2AC1	Fe5-TiO_2AC1	Fe10-TiO_2AC1
pH	6.52	6.76	6.88	6.08
Zeta Potential ± Std. DEV (mV)	−18.0 ± 0.472	−18.2 ± 0.332	−20.1 ± 1.290	−21.9 ± 0.953

The PZC slightly increases for the nanocomposites with iron, except for the Fe10-TiO_2AC1 sample. In this last case, the lower value suggests an enrichment of species exhibiting acidic behavior, such as Fe_2O_3, which appears on the surface, according to the XPS results.

Table S1 compares some results obtained in the photodegradation of CR using catalysts based on TiO_2 and Fe. It is observed that the removal efficiency is influenced by the reaction conditions, the synthesis method, or the precursor used for iron. Even the degree of CR photodegradation is lower under neutral pH conditions for Fe10-TiO_2AC1, at acidic pH, the results correspond to those obtained with other photocatalysts. Similar findings, with a similar catalytic system but another dye, were obtained and explained by the synergism between adsorption and the photocatalytic reaction favored by the acidic pH [83]. At lower pH values, on the surface of photocatalytic composites, CR anions are easily adsorbed and more directly oxidized by hydroxyl radicals produced under light excitation [84].

The activity of the TiO_2ACn and Fex-TiO_2AC1 composites is attributed to the presence of heterojunctions and the associated charge transport between the iron oxide, carbon, and TiO_2 components, which likely suppresses charge recombination. The removal efficiency increases with the amount of iron oxide, from 32.6% for the AC1 support to 66.6% for the Fe10-TiO_2AC1 sample. The higher activity of the TiO_2AC0 sample may be due to oxygen vacancies and a higher carbon concentration on the surface (Table 3). It has been shown previously that the addition of carbon improves the conductivity of TiO_2 by facilitating a charge transfer from within its lattice to the surface, where the photocatalytic reaction takes place [85]. At the same time, the presence of carbon reduces the band gap energy and improves the photocatalytic activity in the presence of visible light (Table 1). However, the carbon addition induces the formation of oxygen vacancies and, consequently, the

appearance of new energy levels near the CB. The electrons from these levels could be excited to CB even by visible light. From PL experiments, the TiO_2AC0 sample has the largest number of oxygen vacancies, which can explain its higher efficiency in photocatalytic reactions. Similar results have been reported in the literature [69,70,86].

To better understand the differences in behavior between the most efficient samples (specifically TiO_2AC0 and Fe10-TiO_2AC1), the absorbance spectra of the CR solution were recorded between 200 and 600 nm during the photodegradation experiments (Figure 10). In aqueous solutions, the CR dye presents two absorption bands at 497 nm ($\pi \rightarrow \pi^*$) and 346 nm ($n \rightarrow \pi^*$). The first peak is associated with transitions characteristic of the azo-group (-N=N-) and the other with transitions in the naphthalene ring [12]. Moreover, the absorbance at 254 nm is directly related to the dissolved organic carbon (DOC). The method has been used since 1962 and standardized since 1995 [87,88]. In the literature, the major intermediates that resulted in CR degradation were detected by LC-MS. It was found that, initially, the two sulfonate groups and the azo bonds were cleaved, with azo bonds being more easily degraded than the aromatic rings [89,90]. The intermediates, mainly composed of naphthalene and aromatic derivatives, were further degraded and oxidized via hydroxyl radicals, producing lower and lower molecular mass intermediates until complete mineralization into CO_2, H_2O, NO_3, and NH_4 [12,89,90]. In Figure 10, it can be observed that TiO_2AC0 can easily degrade azo bonds but not the aromatic rings, while Fe10-TiO_2AC1 has a significantly higher capacity to mineralize the dye.

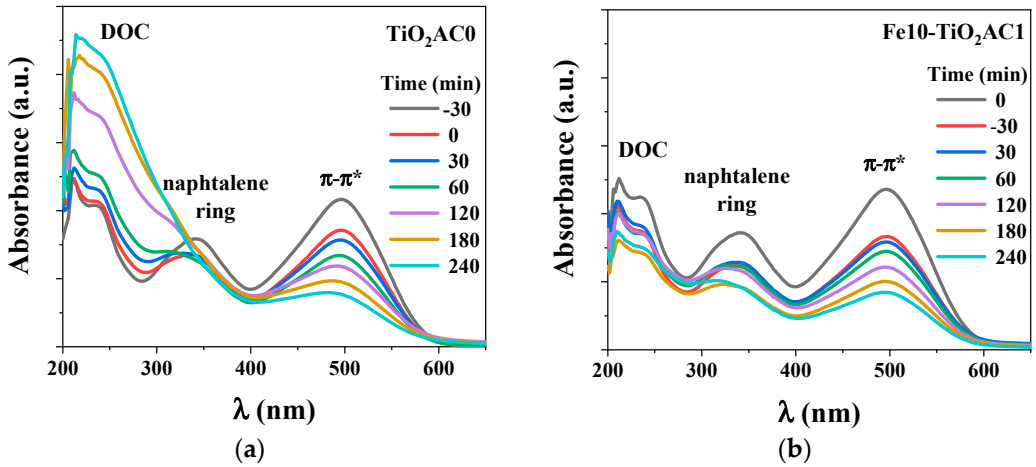


Figure 10. Registered UV-Vis spectra during RC photodegradation over the TiO_2AC0 (**a**) and Fe10-TiO_2AC1 (**b**) photocatalysts.

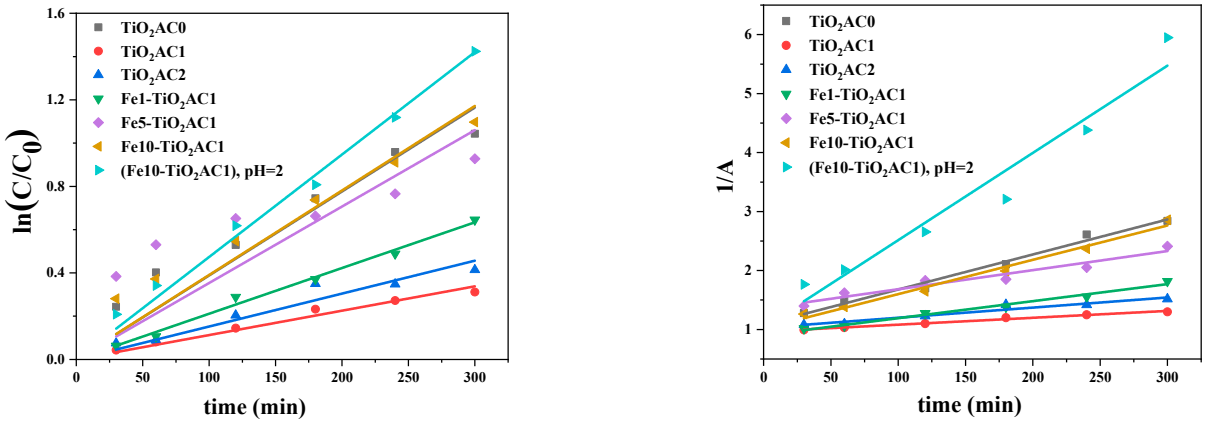
2.2.2. Kinetics of the Photocatalytic Reactions

Two kinetic models were used to investigate the CR photodegradation: pseudo-first-order and pseudo-second-order kinetics, described by the following equations [45,91]:

$$\text{Pseudo-first-order: } \ln(C_0/C) = k_1 t \quad (1)$$

$$\text{Pseudo-second-order: } 1/C = 1/C_0 + k_2 t \quad (2)$$

where C_0 and C are the CR concentrations in the initial solution and after time t, k_1 and k_2 are the rate constants for pseudo-first-order and -second-order reactions, respectively. The results are displayed in Figure 11 and Table 5. Although the zero-order kinetic model was also tested, it did not provide a good fit and is therefore not included here.



(**a**) (**b**)

Figure 11. Kinetic analysis of the photodegradation of CR over various catalysts considering (**a**) first-order and (**b**) second-order mechanisms.

Table 5. Kinetic parameters determined for CR photodegradation over various samples.

Sample	First-Order			Second-Order		
	$k_1 \cdot 10^{-3}$ (min^{-1})	$t_{1/2}$ (min)	R^2	k_2 ($L \cdot mol^{-1} \cdot min^{-1}$) × 10^5	$t_{1/2}$ (min)	R^2
TiO_2AC0	3.88	178.6	0.8677	136.5	182.4	0.9869
TiO_2AC1	1.13	533.1	0.9672	26.89	803.3	0.9868
TiO_2AC2	1.52	455.9	0.9128	39.5	597.3	0.9436
Fe1-TiO_2AC1	2.11	328.4	0.9910	66.4	312.2	0.9842
Fe5-TiO_2AC1	3.53	196.3	0.3717	96.8	273.1	0.9468
Fe10-TiO_2AC1	3.91	177.2	0.8681	133.8	174.7	0.9862
(Fe10-TiO_2AC1), pH = 2	4.70	147.5	0.9882	335.6	65.3	0.9509

Based on the values of the correlation coefficients, it can be concluded that the second-order kinetic model better fits the experimental data. However, the good fit observed for both models suggests that multiple mechanisms are possible [86]. To better characterize the photodegradation ability of the studied samples, the $t_{1/2}$ (the time needed for the concentration of CR to attain half of its value) was also calculated and listed in Table 5. The kinetics of the photocatalytic degradation of Cibacron Yellow F-4G dye on similar Fe-TiO_2/AC composites [83] was analyzed using the second-order and Langmuir-Hinshelwood (L-H) models. The obtained results indicated the L-H model, as the most appropriate to describe the photocatalytic degradation of the CYF-4G dye.

2.2.3. Mechanism of Congo Red Photodegradation

The photogenerated charges (h^+, e^-) and the free radicals produced by them in the presence of water and oxygen on the photocatalyst surface have a significant role in the degradation of organic compounds by facilitating the initiation and propagation of chemical reactions. To investigate the influence of free radicals on the photocatalytic degradation of CR, trapping experiments were performed using potassium iodide, silver nitrate, ethanol, and p-benzoquinone as h^+, e^-, •OH, and $\bullet O_2^-$ scavengers, respectively. The CR degradation experiments, illustrated in Figure 12, were carried out at pH = 6.

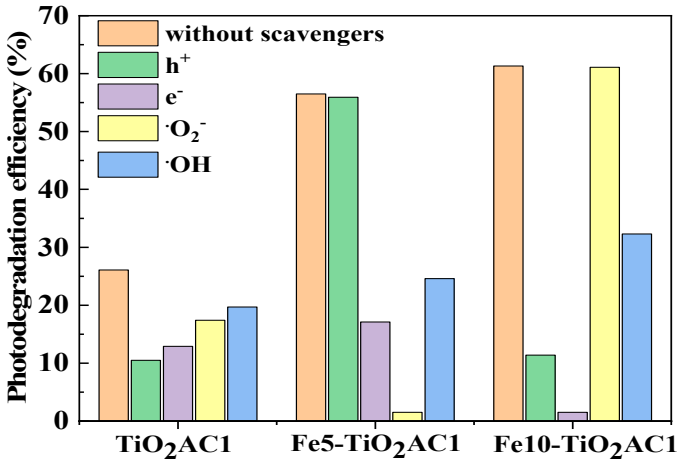


Figure 12. Scavengers experiments for the photocatalytic degradation of CR.

The addition of scavengers to the reaction system, for the TiO_2AC1 sample, led to a distinct decrease in CR photodegradation efficiency, indicating that all active species considered are involved in the process. For the Fe5-TiO_2AC1 sample, a significant decrease in efficiency was observed in the presence of e^-, •OH, and, especially, $•O_2^-$ scavengers. On the contrary, the presence of the h^+ scavenger does not influence the efficiency of CR degradation, indicating that holes do not play a significant role in radical formation and, thus, in the photodegradation process. Unlike this photocatalyst, for which the XPS results indicated only the presence of Fe^{2+}, in the case of the Fe10-TiO_2AC1 sample, no influence of the $•O_2^-$ scavenger was revealed. However, there was a decrease in efficiency in the presence of the h^+, •OH, and, especially, e^- scavengers. It turns out that, in this case, electrons and holes have a significant contribution to the generation of •OH radicals and play a key role in CR photodegradation. From these results, it can be stated that, on the Fe10-TiO_2AC1 nanocomposite, •OH radicals are mainly produced, while, mostly, $•O_2^-$ radicals are produced to degrade CR.

In conclusion, the mechanism of the photocatalytic process is significantly influenced by the iron species immobilized on TiO_2 and on their concentration. In the presence of both Fe^{2+} and Fe^{3+} ions, all reaction steps that generate •OH radicals are favored:

$$h_{VB}^+ + H_2O \rightarrow •OH + H^+ \quad (3)$$

$$e_{CB}^- + O_2 \rightarrow •O_2^- + H_2O \rightarrow HOO• + OH^- \quad (4)$$

$$HOO• + H_2O \rightarrow H_2O_2 + •OH \quad (5)$$

$$h_{VB}^+ + OH^- \rightarrow •OH \quad (6)$$

Considering all of these observations, a degradation mechanism was proposed (Figure 13).

Based on the reported information about the energy levels for the Fe-TiO_2 materials [92,93], two key levels were identified: a reduction level positioned below the TiO_2 conduction band and an oxidation level located above the TiO_2 valence band. Under irradiation with light of a wide wavelength range (400–750 nm), electrons can be activated from both the VBs of TiO_2 and the iron oxides. They can migrate into the CBs of the two oxide phases, generating holes in the VBs. The holes from the VB of TiO_2 can migrate to the VB of the iron oxide. Meanwhile, electrons from the CBs of TiO_2 and iron oxide can migrate to carbon or reduce the Fe^{3+} ions, generating Fe^{2+}. The electrons from the carbon surface and the superficial Fe^{2+} ions interact with the adsorbed oxygen molecules, forming $•O_2^-$ radicals. The holes from the oxidation level can generate iron ions in a higher oxidation state on the surface. Both the holes and the formed iron ions react with the adsorbed H_2O to create •HO radicals. •HO and $•O_2^-$ radicals are mainly responsible for the degradation

of CR dye. In the case of the Fe5-TiO_2AC1 sample, the oxidation processes of Fe^{2+} are favored by the formed holes. Also, the generated electrons are transferred to the available conduction bands and to AC. Thus, a high number of $\bullet O_2^-$ radicals are formed (Figure 13). The presence of both Fe^{2+} and Fe^{3+} (the case of the sample Fe10-TiO_2AC1) favors both the oxidation of Fe^{2+} and of water, with the formation of •OH radicals (Figure 13). Electrons from the conduction bands or AC reduce trivalent iron and, with oxygen dissolved in the water, can generate $\bullet O_2^-$ radicals. In the presence of water, these form •OH radicals according to Reactions (3)–(6).

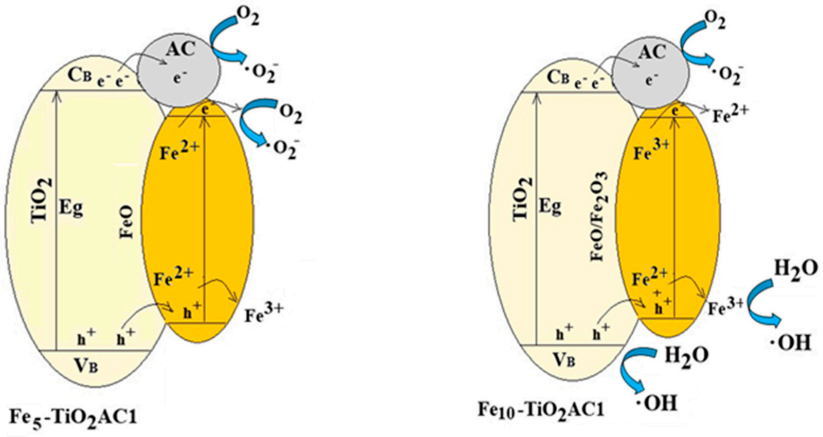


Figure 13. Proposed mechanism for CR photodegradation using Fe-TiO_2AC nanocomposites.

2.2.4. Reusability of the Photocatalysts

The reusability of a photocatalyst is an important characteristic for practical applications. To determine the recyclability of the Fe10-TiO_2AC sample (with the highest photodegradation efficiency and mineralization grade), the reaction for the photodegradation of CR was repeated up to three times. Each cycle was performed at a pH of 6 for 300 min. After each cycle, the Fe10-TiO_2AC1 sample was separated by centrifugation, washed with distilled water, dried overnight at 70 °C, and then used for the next reaction cycle.

The results presented in Figure 14 show that the removal efficiency did not vary significantly after three experimental cycles, indicating that the nanocomposite remained stable under experimental conditions. The recyclability test confirmed that no leaching of Ti and Fe ions was observed after three successful reaction cycles carried out in the condition of pH = 6.

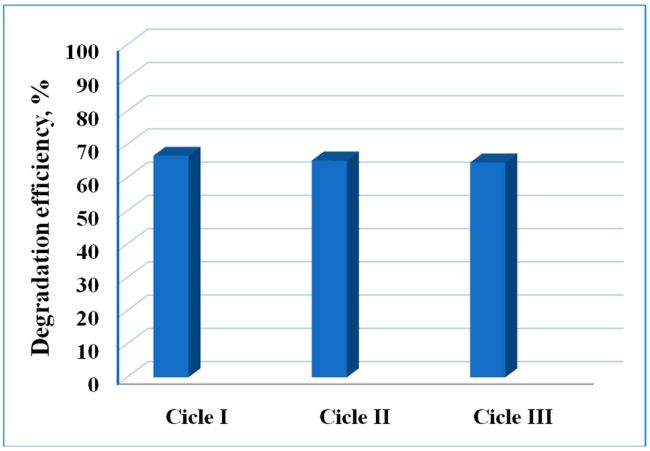


Figure 14. Reusability of the Fe10-TiO_2AC1 sample in the photodegradation of the CR aqueous solution (5×10^{-5} M) under visible irradiation for 5 h per cycle.

3. Materials and Methods

3.1. Materials

Titanium (IV) isopropoxide (Fluka) was the titanium precursor; Brij-58 ($C_{16}H_{33}O(CH_2CH_2O)_2OH$) from Merck (Rahway, NJ, USA) was a non-ionic surfactant. Other materials used in the synthesis were hydrochloric acid (37%), orto-phosphoric acid (85%) from Merck and isopropyl alcohol from Sigma-Aldrich (St. Louis, MO, USA). Dye degraded in the photocatalytic tests was Congo red from Merck.

3.2. Synthesis of Materials

3.2.1. TiO_2-AC Composites

Two activated carbon samples were obtained from coffee grounds washed with distilled water and dried 24 h at 60 °C. The coffee grounds were dispersed into orto-phosphoric acid solution (coffee/acid mass ratio of 1/3) and separated by filtration, as we reported previously [15]. The obtained solid was then washed with different amounts of hot distilled water (20; respectively, 10 water/solid mass ratio). The samples obtained after pyrolysis at 450 °C were named AC0 and AC, respectively. TiO_2AC composites were obtained by the sol–gel method starting from Ti isopropoxide, AC and Brij 58, a non-ionic surfactant (Figure 15). The TiO_2AC0 sample was prepared with AC0 and two others (TiO_2AC1, TiO_2AC2) with AC varying the Ti alkoxide/AC mass ratio (14 and 16, respectively).



Figure 15. Diagram of the nanocomposite samples preparation.

In the first step, mixture A was obtained as follows: 4.5 g Brij was dispersed in 20 mL of HCl solution (0.1 N) and stirred 2 h at 40 °C. During this time, AC was dispersed in a 175 mL solution of Ti isopropoxide in isopropyl alcohol (0.4 M) by stirring at 40 °C for 1 h (mixture B). In the second step, mixture B was dropwise added to mixture A. The resulting sol was stirred for 4 h at room temperature, transferred to a Petri dish and kept for 24 h. A gel was obtained, which was then dried at 80 °C for 24 h and calcined in air at 450 °C (rate 2 °C/min) for 6 h (Figure 15).

3.2.2. Fe-TiO_2AC1 Samples

The nanocomposite photocatalysts were obtained by TiO_2AC1 impregnation with an aqueous solution of $Fe(NO_3)_3$. The concentration of iron precursor solution was calculated to obtain photocatalysts with 1, 5, and 10 wt.% Fe_2O_3. After impregnation, the materials were kept for 24 h at room temperature and dried for another 24 h at 80 °C. Finally, they were calcined at 450 °C for 6 h, and the following samples: Fe1-TiO_2AC, Fe5-TiO_2AC, and Fe10-TiO_2AC were prepared.

3.3. Characterization of Materials

The samples' crystalline structure was obtained with the aid of a Bruker D2 Phaser diffractometer (Billerica, MA, USA) in Bragg-Brentano theta-theta geometry using CuKα1 radiation (λ = 1.5406 Å). The scanning range was 15° to 80° (in 2θ) with an increment of 0.04°.

The morphology of the catalysts was followed with a scanning electron microscope FEI Quanta 3D FEG (FEI, Brno, Czech Republic) operating at an accelerating voltage of 5 kV without coating.

The specific surface area (S_{BET}) and pore structure were measured by nitrogen physisorption at −196 °C using a Micromeritics ASAP 2020 automated gas adsorption analyzer (Norcross, GA, USA). The samples were degassed at 200 °C for 4 h under vacuum before analysis.

Raman spectra were recorded at room temperature using a LabRam HR 800 spectrometer (Horiba France SAS, Palaiseau, France) over the 200–2000 cm^{-1} range. Samples were excited with a 325 nm laser line (from Kimmon Koha Co., LTD., Tokyo, Japan) to throw an Olympus objective of 40 × NUV/0.47 (Olympus Corporation, Tokyo, Japan) with a spot size smaller than 1 μm.

Elemental analysis of the samples was performed in a vacuum using a Rigaku ZSX Primus II spectrometer (Tokyo, Japan). The results were analyzed using EZ-scan combined with Rigaku SQX fundamental parameters software (version 5.18).

X-ray photoelectron spectroscopy (XPS) was carried out on Thermo Fisher EscaLab 250Xi+ equipment (Waltham, MA, USA) with a thin anode (Al and Ag). The monochromatized 1486.6 eV Al Kα line with a beam diameter adjusted at 900 μm was used as the X-ray source.

The vibrational spectra (FTIR) were recorded with a Jasco FT/IR-4700 spectrophotometer (Tokyo, Japan) and ATR-FTIR spectroscopy by the Nicolet iS10 FT-IR spectrometer (Thermo Scientific, Waltham, MA, USA) covering the range of 4000 to 600 cm^{-1}. The spectra were acquired with an average of 32 scans with a spectral resolution of 4 cm^{-1} in attenuated total reflectance (ATR) mode.

The PL spectra were obtained using a FLSP920 fluorimeter from Edinburgh Instruments (Livingston, UK). The excitation wavelength was 350 nm. The slits for all measurements were 8 nm for excitation and 8 nm for emission.

The DR UV–Vis spectra were registered in the 900–200 nm range using a Perkin Elmer Lambda 35 spectrophotometer (Shelton, CT, USA). The reflectance data were converted in absorbance using the Kubelka–Munk function.

The particle size distribution and the zeta potential (ZP or ζ) of the oxide powders suspended in water was determined by dynamic light scattering (DLS) using Malvern Zeta Sizer Nano-ZS equipment (Malvern Instruments, Malvern, UK). The measurements were performed at 25 °C, considering the properties of double-distilled water used in solution preparations, standard viscosity of 0.8872 cP, refractive index of 1.330, and dielectric constant of 78.5.

3.4. Photocatalytic Reactions

The photodegradation experiments were carried out at room temperature in glass reactors containing 20 mL aqueous solutions of CR dye (5×10^{-5} M concentration) and 10 mg of photocatalyst. The mixture was continuously stirred with a magnetic stirrer. To ensure the adsorption/desorption equilibrium, the suspension was initially kept in the dark for 30 min. Then, a visible light (LED source: 400–750 nm, 24 W, luminous flux 2700 lm) was used to irradiate the solution, and 2.5 mL of suspension was withdrawn at various times, centrifuged and analyzed using a Perkin Elmer Lambda 35 UV–Vis spectrophotometer. The photocatalytic activity of the samples was quantitatively evaluated by determining the degradation efficiency (η%) based on the equation:

$$\eta = [(C_0 - C)/C_0] \times 100$$

where C_0 represents the concentration of the dye solutions measured before irradiation, and C is the concentration of the dye solutions at time t at the 498 nm wavelength.

For the scavenger experiments, 0.1 mmol of potassium iodide, silver nitrate, ethanol and p-benzoquinone were added to the CR solution as h^+, e^-, •OH and $\bullet O_2^-$ scavengers, respectively. The procedure was similar to the photocatalytic experiments. The results were obtained after 5 h of irradiation.

The leaching was evaluated as follows: 10 mg of catalyst, introduced into 20 mL HCl aqueous solution with pH = 2, was irradiated 5 h under similar conditions with photocatalytic reactions. After this treatment, the solid was separated by centrifugation and filtration, and 2 mL of the filtrate were mixed with 0.5 mL of salicylic acid solution (0.002 M). The intensity of the maximum absorption at 560 nm was compared to that of an iron nitrate solution (3.14×10^{-4} M).

4. Conclusions

In this research were obtained nanocomposites active and stable in photocatalytic degradation under visible light of Congo red dye in water. The materials containing anatase and phosphorus activated carbon were synthesized using the sol–gel method in the presence of Brij 58 as the surfactant. The sample with a higher surface area (185.6 m^2/g) was promoted with iron in different loadings by impregnation with iron nitrate solution. The presence of carbon has a significant influence on the composite material texture, whereas iron oxide has a less pronounced effect. A high value of the efficiency in Congo red degradation was obtained in the case of the TiO_2AC nanocomposite with a higher C percent on the surface and without P. Therefore, carbon induced new electronic sites, and the photoluminescence spectra evidenced for this sample the largest number of oxygen vacancies, which can explain its higher efficiency in the photocatalytic reaction. The XPS results mainly indicated the presence of Fe^{2+} for the samples with a lower iron content (0.83%, 3.30%), while, for 7.17% Fe, both Fe^{2+} and Fe^{3+} were evidenced. These differences in surface composition influenced both the mechanism of the photocatalytic reactions and the efficiency of the dye degradation in water. Thus, the proposed mechanisms, based on the results obtained in the presence of scavengers, showed a significant effect of $\bullet O_2^-$ and OH• radicals in the photodegradation of Congo red using samples with lower and higher iron contents, respectively. Degradation processes can be well-fitted with the second-order kinetics model. The higher values of dye degradation efficiency were obtained for the sample with the higher iron content. Moreover, the samples containing Fe showed a higher tendency to mineralize the dye. Nevertheless, the best result (85% efficiency) was in acidic conditions. However, in these pH conditions 1.6% iron leaching was observed. Therefore, the synthesized Fe-TiO_2AC nanocomposites exhibit high potential in photocatalytic degradation of the dyes from the textile industry under visible light.

Supplementary Materials: The following supporting information can be downloaded at: https://www.mdpi.com/article/10.3390/catal14120844/s1, Figure S1: SEM images of the TiO_2AC0 (a), TiO_2AC1 (b) and TiO_2AC2 (c) samples; Figure S2: High-resolution XPS spectra of Ti2p for the TiO_2AC1 samples; Figure S3: High-resolution XPS spectra of Ti2p for the Fex-TiO_2AC1 samples; Figure S4: High-resolution XPS spectra of O1s for the TiO_2ACn samples. Figure S5: High-resolution XPS spectra of O1s for the Fex-TiO_2AC1 samples; Figure S6: High-resolution XPS spectra of C1s for the TiO_2ACn samples; Figure S7: High-resolution XPS spectra of C1s for the Fex-TiO_2AC1 samples; Figure S8: High-resolution XPS spectra of P2p for the Fex-TiO_2AC1 samples; Figure S9: The band gap energies (Eg) determined from Tauc plots by direct (a) and indirect (b) transitions; Figure S10: Molecular structure of Congo Red dye; Figure S11: Congo Red adsorption isotherms for the nanocomposite materials; Figure S12: Congo Red photodegradation under visible irradiation and pH = 6, except Fe10-TiO_2AC1, for which the reaction was also carried out at pH = 2; Figure S13: The average result for fifteen values of zeta potential measurements and the corresponding standard error; Table S1: Congo Red dye photodegradation over different photocatalysts [12,84,89,94,95].

Author Contributions: D.N.: Conceptualization, Investigation, Methodology, Validation and Writing—original draft; V.B.: Investigation, Methodology, Validation, Writing—original draft and Writing—

review and editing; M.G.: Investigation, Formal analysis and Validation; I.A.: Investigation, Formal analysis and Validation; D.C.C.: Investigation, Formal analysis and Validation; A.N.: Investigation, Formal analysis and Validation; A.B.: Investigation and Formal analysis; S.P.: Investigation, Formal analysis and Validation; V.P.: Conceptualization, Methodology, Investigation, Supervision, Validation, Formal analysis, Writing—original draft and Writing—review and editing. All authors have read and agreed to the published version of the manuscript.

Funding: This research received no external funding.

Data Availability Statement: The data presented in this study are available on request from the corresponding author.

Conflicts of Interest: The authors declare no conflicts of interest.

References

1. Khan, S.; Malik, A. Environmental and health effects of textile industry wastewater. In *Environmental Deterioration and Human Health: Natural and Anthropogenic Determinants*; Malik, A., Grohmann, E., Akhtar, R., Eds.; Springer: Dordrecht, The Netherlands, 2014; pp. 55–71.
2. Wang, X.; Jiang, J.; Gao, W. Reviewing textile wastewater produced by industries: Characteristics, environmental impacts, and treatment strategies. *Water Sci. Technol.* **2022**, *85*, 2076–2096. [CrossRef]
3. Islam, T.; Repon, M.R.; Islam, T.; Sarwar, Z.; Rahman, M.M. Impact of textile dyes on health and ecosystem: A review of structure, causes, and potential solutions. *Environ. Sci. Pollut. Res.* **2023**, *30*, 9207–9242. [CrossRef] [PubMed]
4. Zaharia, C.; Suteu, D. Textile organic dyes—Characteristics, polluting effects and separation/elimination procedures from industrial effluents—A critical overview. In *Organic Pollutants Ten Years After the Stockholm Convention—Environmental and Analytical Update*; Puzyn, T., Mostrag-Szlichtyng, A., Eds.; IntechOpen: Rijeka, Croatia, 2012; Volume 3, pp. 55–86.
5. Zainith, S.; Sandhya, S.; Saxena, G.; Bharagava, R. Microbes: An eco-friendly tools for the treatment of industrial wastewaters. In *Microbes and Environmental Management*; Singh, J.S., Singh, D.P., Eds.; Studium Press: New Delhi, India, 2016; pp. 75–100.
6. Pereira, L.; Alves, M. Dyes—Environmental Impact and Remediation. In *Environmental Protection Strategies for Sustainable Development, Strategies for Sustainability*; Malik, A., Grohmann, E., Eds.; Springer Science + Business Media, B.V.: Dordrecht, The Netherlands, 2012; pp. 111–154.
7. Das, A.; Mishra, S. Removal of textile dye reactive green-19 using bacterial consortium: Process optimization using response surface methodology and kinetics study. *J. Environ. Chem. Eng.* **2017**, *5*, 612–627. [CrossRef]
8. Khor, C.M.; Khan, M.M.; Harunsani, M.H. Silver Niobate-based Photocatalysts: Relevance in Dye Degradation. *Chem. Phys. Impact.* **2022**, *6*, 100141. [CrossRef]
9. Mathur, N.; Bhatnagar, P.; Bakre, P. Assessing mutagenicity of textile dyes from Pali (Rajasthan) using Ames bioassay. *Appl. Ecol. Environ. Res.* **2006**, *4*, 111–118. [CrossRef]
10. Lellis, B.; Fávaro-Polonio, C.Z.; Pamphile, J.A.; Polonio, J.C. Effects of textile dyes on health and the environment and bioremediation potential of living organisms. *Biotechnol. Res. Innov.* **2019**, *3*, 275–290. [CrossRef]
11. Mani, S.; Chowdhary, P.; Bharagava, R.N. Textile wastewater dyes: Toxicity profile and treatment approaches. In *Emerging and Eco-Friendly Approaches for Waste Management*; Bharagava, R.N., Chowdhary, P., Eds.; Springer: Singapore, 2019; pp. 219–244.
12. Zafar, Z.; Ali, I.; Park, S.; Kim, J.O. Effect of different iron precursors on the synthesis and photocatalytic activity of Fe–TiO_2 nanotubes under visible light. *Ceram. Int.* **2020**, *46*, 3353–3366. [CrossRef]
13. Pavel, M.; Anastasescu, C.; State, R.N.; Vasile, A.; Papa, F.; Balint, I. Photocatalytic degradation of organic and inorganic pollutants to harmless end products: Assessment of practical application potential for water and air cleaning. *Catalysts* **2023**, *13*, 380. [CrossRef]
14. Deng, Y.; Zhao, R. Advanced oxidation processes (AOPs) in wastewater treatment. *Curr. Pollut. Rep.* **2015**, *1*, 167–176. [CrossRef]
15. Negoescu, D.; Atkinson, I.; Gherendi, M.; Culita, D.C.; Baran, A.; Petrescu, S.; Trica, B.; Pelinescu, D.; Ionescu, R.; Bratan, V.; et al. Brij 58–activated carbon assisted synthesis of Ag/Ag_2O/TiO_2-AC photocatalysts for efficient organic pollutants degradation. *J. Alloys Compd.* **2023**, *931*, 167528. [CrossRef]
16. Hammud, H.H.; Traboulsi, H.; Karnati, R.K.; Bakir, E.M. Photodegradation of Congo Red by Modified P25-Titanium Dioxide with Cobalt-Carbon Supported on SiO_2 Matrix, DFT Studies of Chemical Reactivity. *Catalysts* **2022**, *12*, 248. [CrossRef]
17. Mureseanu, M.; Chivu, V.; Osiac, M.; Ciobanu, M.; Bucur, C.; Parvulescu, V.; Cioatera, N. New photoactive mesoporous Ce-modified TiO_2 for simultaneous wastewater treatment and electric power generation. *Catal. Today* **2021**, *366*, 164–176. [CrossRef]
18. Armaković, S.J.; Savanović, M.M.; Armaković, S. Titanium dioxide as the most used photocatalyst for water purification: An overview. *Catalysts* **2022**, *13*, 26. [CrossRef]
19. Carp, O.; Huisman, C.L.; Reller, A. Photoinduced reactivity of titanium dioxide. *Prog. Solid State Chem.* **2004**, *32*, 33–177. [CrossRef]

20. Predoană, L.; Ciobanu, E.M.; Petcu, G.; Preda, S.; Pandele-Cușu, J.; Anghel, E.M.; Petrescu, S.V.; Culita, D.C.; Baran, A.; Surdu, V.-A.; et al. Photocatalytic Performance of Sn–Doped TiO_2 Nanopowders for Photocatalytic Degradation of Methyl Orange Dye. *Catalysts* **2023**, *13*, 534. [CrossRef]
21. Kao, L.H.; Hsu, T.; Lu, H. Sol–gel synthesis and morphological control of nanocrystalline TiO_2 via urea treatment. *J. Colloid Interface Sci.* **2007**, *316*, 160–167. [CrossRef] [PubMed]
22. Mori, K.; Maki, K.; Kawasaki, S.; Yuan, S.; Yamashita, H. Hydrothermal synthesis of TiO_2 photocatalysts in the presence of NH_4F and their application for degradation of organic compounds. *Chem. Eng. Sci.* **2008**, *63*, 5066–5070. [CrossRef]
23. Naseem, K.; Farooqi, Z.H.; Begum, R.; Irfan, A. Removal of Congo red dye from aqueous medium by its catalytic reduction using sodium borohydride in the presence of various inorganic nano-catalysts: A review. *J. Clean. Prod.* **2018**, *187*, 296–307. [CrossRef]
24. Katheresan, V.; Kansedo, J.; Lau, S.Y. Efficiency of various recent wastewater dye removal methods: A review. *J. Environ. Chem. Eng.* **2018**, *6*, 4676–4697. [CrossRef]
25. Preda, S.; Pandele-Cușu, J.; Petrescu, S.V.; Ciobanu, E.M.; Petcu, G.; Culiță, D.C.; Apostol, N.G.; Costescu, R.M.; Raut, I.; Constantin, M.; et al. Photocatalytic and Antibacterial Properties of Doped TiO_2 Nanopowders Synthesized by Sol–Gel Method. *Gels* **2022**, *8*, 673. [CrossRef]
26. Hou, J.; Zhou, J.; Liu, Y.; Yang, Y.; Zheng, S.; Wang, Q. Constructing Ag_2O nanoparticle modified TiO_2 nanotube arrays for enhanced photocatalytic performances. *J. Alloys Compd.* **2020**, *849*, 56493. [CrossRef]
27. Suwanchawalit, C.; Wongnawa, S.; Sriprang, P.; Meanha, P. Enhancement of the photocatalytic performance of Ag-modified TiO_2photocatalyst under visible light. *Ceram. Int.* **2012**, *38*, 5201–5207. [CrossRef]
28. Ismail, A.A.; Bahnemann, D.W.; Bannat, I.; Wark, M. Gold nanoparticles on mesoporous interparticle networks of titanium dioxide nanocrystals for enhanced photonic efficiencies. *J. Phys. Chem. C* **2009**, *113*, 7429–7435. [CrossRef]
29. Gomes Silva, C.; Juárez, R.; Marino, T.; Molinari, R.; García, H. Influence of excitation wavelength (UV or visible light) on the photocatalytic activity of titania containing gold nanoparticles for the generation of hydrogen or oxygen from water. *J. Am. Chem. Soc.* **2011**, *133*, 595–602. [CrossRef]
30. Rosseler, O.; Shankar, M.V.; Karkmaz-Le Du, M.; Schmidlin, L.; Keller, N.; Keller, V. Solar light photocatalytic hydrogen production from water over Pt and Au/TiO_2 (anatase/rutile) photocatalysts: Influence of noble metal and porogen promotion. *J. Catal.* **2010**, *269*, 179–190. [CrossRef]
31. Xue, J.; Bao, J. Interfacial charge transfer of heterojunction photocatalysts: Characterization and calculation. *Surf. Interfaces* **2010**, *25*, 101265. [CrossRef]
32. Thambiliyagodage, C.; Usgodaarachchi, L. Photocatalytic activity of N, Fe and Cu co-doped TiO_2 nanoparticles under sunlight. *Curr. Res. Green Sustain. Chem.* **2021**, *4*, 100186. [CrossRef]
33. Saygi, H.; Ünal, E.; Çakan, A.; Akbay, E. Tailored transition metal-doped TiO_2@Fe_3O_4 nanohybrids for efficient photocatalytic dye removal: Optimization via neural networks and response surface approaches. *Mater Today Sustain.* **2024**, *27*, 100845. [CrossRef]
34. Zhang, Q.; Yu, L.; Yang, B.; Xu, C.; Zhang, W.; Xu, Q.; Diao, G. Magnetic Fe_3O_4@Ru-doped TiO_2 nanocomposite as a recyclable photocatalyst for advanced photodegradation of methylene blue in simulated sunlight. *Chem. Phys. Lett.* **2021**, *774*, 138609. [CrossRef]
35. Kong, X.; Li, J.; Yang, C.; Tang, Q.; Wang, D. Fabrication of Fe_2O_3/g-C_3N_4@N-TiO_2 photocatalyst nanotube arrays that promote bisphenol A photodegradation under simulated sunlight irradiation. *Sep. Purif. Technol.* **2020**, *248*, 116924. [CrossRef]
36. Iqbal, S.; Liu, J.; Ma, H.; Liu, W.; Zuo, S.; Yu, Y. Fabrication of TiO_2/Fe_2O_3/g-C_3N_4 ternary photocatalyst via a low-temperature calcination and solvothermal route and its visible light assisted photocatalytic properties. *J. Mol. Struct.* **2023**, *1282*, 135166. [CrossRef]
37. Husien, S.; El-taweel, R.M.; Salim, A.I.; Fahim, I.S.; Said, L.A.; Radwan, A.G. Review of activated carbon, adsorbent material for textile dyes removal: Preparation, and modelling. *Curr. Res. Green Sustain. Chem.* **2022**, *5*, 100325. [CrossRef]
38. Younas, U.; Gulzar, A.; Ali, F.; Pervaiz, M.; Ali, Z.; Khan, S.; Saeed, Z.; Ahmed, M.; Alothman, A.A. Antioxidant and Organic Dye Removal Potential of Cu-Ni Bimetallic Nanoparticles Synthesized Using *Gazania rigens* Extract. *Water* **2021**, *13*, 2653. [CrossRef]
39. Chi, W.; Yu, F.; Dong, G.; Bai, L.; Guo, D.; Chai, D.-F.; Zhao, M.; Li, J.; Zhang, W. Improved photocatalytic property of ZnO by simultaneously integrating with Ag_3VO_4 for constructing a heterojunction and biochar as charge transfer bridge via microwave hydrothermal method. *J. Environ. Chem. Eng.* **2024**, *12*, 113201. [CrossRef]
40. Chi, W.; Yu, F.; Dong, G.; Zhang, W.; Chai, D.-F.; Han, P.; Zhao, M.; Li, J.; Zhang, X. A novel peony-shaped ZnO/biochar nanocomposites with dominant {100} facets for efficient adsorption and photocatalytic removal of refractory contaminants. *Colloids Surf. A Physicochem. Eng. Asp.* **2024**, *695*, 134291. [CrossRef]
41. Ahmad, A.; Javed, M.S.; Khan, S.; Almutairi, T.M.; Mohammed, A.A.A.; Luque, R. Green synthesized Ag decorated CeO_2 nanoparticles: Efficient photocatalysts and potential antibacterial agents. *Chemosphere* **2023**, *310*, 136841. [CrossRef]
42. Wang, X.; Xue, X.; Liu, X.; Xing, X.; Li, Q.; Yang, J. Synergistic effect of single-electron-trapped oxygen vacancies and carbon species on the visible light photocatalytic activity of carbon-modified TiO_2. *Mater. Chem. Phys.* **2015**, *153*, 117–126. [CrossRef]
43. Cheng, H.; Zhang, W.; Liu, X.; Tang, T.; Xiong, J. Fabrication of titanium dioxide/carbon fiber (TiO_2/CF) composites for removal of methylene blue (MB) from aqueous solution with enhanced photocatalytic activity. *J. Chem.* **2021**, *2021*, 9986158. [CrossRef]
44. Peñas-Garzón, M.; Gómez-Avilés, A.; Belver, C.; Rodriguez, J.J.; Bedia, J. Degradation pathways of emerging contaminants using TiO_2-activated carbon heterostructures in aqueous solution under simulated solar light. *J. Chem. Eng.* **2020**, *392*, 124867. [CrossRef]

45. Matias, M.L.; Pimentel, A.; Reis-Machado, A.S.; Rodrigues, J.; Deuermeier, J.; Fortunato, E.; Martins, R.; Nunes, D. Enhanced Fe-TiO_2 solar photocatalysts on porous platforms for water purification. *Nanomaterials* **2022**, *12*, 1005. [CrossRef]
46. Khlyustova, A.; Sirotkin, N.; Kusova, T.; Kraev, A.; Titov, V.; Agafonov, A. Doped TiO_2: The effect of doping elements on photocatalytic activity. *Mater. Adv.* **2020**, *1*, 1193–1201. [CrossRef]
47. Komaraiah, D.; Radha, E.; Kalarikkal, N.; Sivakumar, J.; Reddy, M.R.; Sayanna, R. Structural, optical and photoluminescence studies of sol-gel synthesized pure and iron doped TiO_2 photocatalysts. *Ceram. Int.* **2019**, *45*, 25060–25068. [CrossRef]
48. Liu, Z.; Wang, G.; Li, Y.; Li, H.; Deng, N. Carboxymethyl-β-cyclodextrin functionalized TiO_2@Fe_3O_4@RGO magnetic photocatalyst for efficient photocatalytic degradation of tetracycline under visible light irradiation. *J. Environ. Chem. Eng.* **2024**, *12*, 113303. [CrossRef]
49. Filip, M.; Petcu, G.; Anghel, E.; Petrescu, S.; Trica, B.; Osiceanu, P.; Stanica, N.; Atkinson, I.; Munteanu, C.; Mureseanu, M.; et al. FeTi- SBA-15 magnetic nanocomposites with photocatalytic properties. *Catal. Today* **2021**, *366*, 10–19. [CrossRef]
50. Lopez, J.; Rey, A.; Vinuelas-Zahinos, E.; Alvarez, P.M. Preparation of a new green magnetic Fe_3O_4@TiO_2-P25 photocatalyst for solar advanced oxidation processes in water. *J. Environ. Chem. Eng.* **2023**, *11*, 109999. [CrossRef]
51. Tumbelaka, R.M.; Istiqomah, N.I.; Kato, T.; Oshima, D.; Suharyadi, E. High reusability of green-synthesized Fe_3O_4/TiO_2 photocatalyst nanoparticles for efficient degradation of methylene blue dye. *Mater. Today Comm.* **2022**, *33*, 104450. [CrossRef]
52. Madima, N.; Kefeni, K.K.; Kuvarega, A.T.; Mishra, S.B.; Mishra, A.K. Visible-light-driven Z-scheme ternary Fe_3O_4/TiO_2/g-C_3N_4 nanocomposite as reusable photocatalyst for efficient removal of dyes and chromium in water. *Mater. Chem. Phys.* **2023**, *296*, 127233. [CrossRef]
53. Wang, C.; Jiao, H.; Yang, Y.; Wu, Y.; Na, P. Dual-Functional S-Scheme Fe_3O_4/TiO_2/g-C_3N_4 double-heterostructure bridged by TiO_2 for collaborative removal of U(VI) and Sb(III). *J. Clean. Prod.* **2023**, *426*, 139114. [CrossRef]
54. Hoseini, A.; Yarmand, B. Enhanced photocatalytic performance and photocorrosion stability of PEO-immobilized TiO_2 photocatalyst using rGO/Fe_2O_3 sensitizers. *Surf. Interfac.* **2023**, *42*, 103424.
55. Gloria, D.C.S.; Brito, C.H.V.; Mendonça, T.A.P.; Brazil, T.R.; Domingues, R.A.; Vieira, N.C.S.; Santos, E.B.; Gonçalves, M. Preparation of TiO_2/activated carbon nanomaterials with enhanced photocatalytic activity in paracetamol degradation. *Mater. Chem. Phys.* **2023**, *305*, 127947. [CrossRef]
56. Ali, S.; Zhijun Li, Z.; Chen, S.; Zada, A.; Khan, I.; Khan, I.; Ali, W.; Shaheen, S.; Qu, Y.; Jing, L. Synthesis of activated carbon-supported TiO_2-based nano-photocatalysts with well recycling for efficiently degrading high-concentration pollutants. *Catal. Today* **2019**, *335*, 557–564. [CrossRef]
57. Mondol, B.; Sarker, A.; Shareque, A.M.; Dey, S.C.; Islam, M.T.; Das, A.K.; Shamsuddin, S.M.; Molla, M.A.I.; Sarker, M. Preparation of Activated Carbon/TiO_2 Nanohybrids for Photodegradation of Reactive Red-35Dye Using Sunlight. *Photochem* **2021**, *1*, 54–66. [CrossRef]
58. Eitel, D.; Graml, J.; Hoppe, J.; Kaliwoda, M.; Hornfeck, M.; Helbig, U. Synthesis and Structure of Carbon-doped TiO_2 by Carbothermal Treatment. *Nano Select.* **2023**, *4*, 454–461. [CrossRef]
59. Inagaki, M.; Hirose, Y.; Matsunaga, T.; Tsumura, T.; Toyoda, M. Carbon coating of anatase-type TiO_2 through their precipitation in PVA aqueous solution. *Carbon* **2003**, *41*, 2619–2624. [CrossRef]
60. Ren, W.; Ai, Z.; Jia, F.; Zhang, L.; Fan, X.; Zou, Z. Low temperature preparation and visible light photocatalytic activity of mesoporous carbon-doped crystalline TiO_2. *Appl. Catal. B Environ.* **2007**, *69*, 138–144. [CrossRef]
61. Ji, L.; Zhang, Y.; Miao, S.; Gong, M.; Liu, X. In situ synthesis of carbon doped TiO_2 nanotubes with an enhanced photocatalytic performance under UV and visible light. *Carbon* **2017**, *125*, 544–550. [CrossRef]
62. Craciun, E.; Predoana, L.; Atkinson, I.; Jitaru, I.; Anghel, E.M.; Bratan, V.; Gifu, C.; Anastasescu, C.; Rusu, A.; Raditoiu, V.; et al. Fe^{3+}-doped TiO_2 nanopowders for photocatalytic mineralization of oxalic acid under solar light irradiation. *J. Photochem. Photobiol. A Chem.* **2018**, *356*, 18–28. [CrossRef]
63. Singha, A.; Bhaduri, K.; Kothari, A.C.; Chowdhury, B. Selective hydroxylation of benzene to phenol via C–H activation over mesoporous Fe_2O_3-TiO_2 using H_2O_2. *Mol. Catal.* **2022**, *533*, 112800. [CrossRef]
64. Zarafu, I.; Turcu, I.; Culita, D.C.; Petrescu, S.; Popa, M.; Chifiriuc, M.C.; Limban, C.; Telehoiu, A.; Ionita, P. Antimicrobial Features of Organic Functionalized Graphene-Oxide with Selected Amines. *Materials* **2018**, *11*, 1704. [CrossRef]
65. Tabakova, T.; Nikolova, D.; Ivanov, I.; Anghel, E.M.; Karashanova, D.; Karakirova, Y.; Venezia, A.M.; Vakros, J.; Crisan, M.; Tenchev, K.; et al. Study of ceria-doped Au/TiO_2 catalysts for boosting hydrogen production by water-gas shift reaction. *Int. J. Hydrogen Energy.* **2024**, *70*, 389–403. [CrossRef]
66. Musat, V.; Stanica, N.; Anghel, E.M.; Atkinson, I.; Culita, D.C.; Polosan, S.; Crintea, L.; Cantaragiu Ceoromila, A.; Buruiana, C.-T.; Carp, O. Magnetic Core-Shell Iron Oxides-Based Nanophotocatalysts and Nanoadsorbents for Multifunctional Thin Films. *Membranes* **2022**, *12*, 466. [CrossRef] [PubMed]
67. Krishnan, P.; Liu, M.; Itty, P.; Liu, Z.; Rheinheimer, V.; Zhang, M.-H.; Monteiro, P.J.M.; Yu, L.E. Characterization of photocatalytic TiO_2 powder under varied environments using near ambient pressure X-ray photoelectron spectroscopy. *Sci. Rep.* **2017**, *7*, 43298. [CrossRef]
68. Varnagiris, S.; Medvids, A.; Lelis, M.; Milcius, D.; Antuzevics, A. Black carbon-doped TiO_2 films: Synthesis, characterization and photocatalysis. *J. Photochem. Photobiol. A Chem.* **2019**, *382*, 111941. [CrossRef]
69. Wang, X.; Tang, Y.; Leiw, M.-Y.; Lim, T.-T. Solvothermal synthesis of Fe-C codoped TiO2 nanoparticles for visible-light photocatalytic removal of emerging organic contaminants in water. *Appl. Catalysis A Gen.* **2011**, *409–410*, 257–266. [CrossRef]

70. Li, Y.; Chen, J.; Liu, J.M.; Ma, M.; Chen, W.; Li, L. Activated carbon supported TiO_2-photocatalysis doped with Fe ions for continuous treatment of dye wastewater in a dynamic reactor. *J. Environ. Sci.* **2010**, *22*, 1290–1296. [CrossRef]
71. Munoz, R.; Sanchez-Sanchez, C.; Merino, P.; Lopez-Elvira, E.; Munuera, C.; Gant, P.; Lopez, M.F.; Castellanos-Gomez, A.; Martin-Gago, J.A.; Garcia-Hernandez, M. Tailored graphenic structures directly grown on titanium oxide boost the interfacial charge transfer. *Appl. Surf. Sci.* **2020**, *504*, 144439. [CrossRef]
72. Gupta, R.P.; Sen, S.K. Calculation of multiplet structure of core *p*-vacancy levels. *Phys. Rev. B* **1974**, *10*, 7. [CrossRef]
73. Gupta, R.P.; Sen, S.K. Calculation of multiplet structure of core *p*-vacancy levels. II. *Phys. Rev. B* **1975**, *12*, 15. [CrossRef]
74. Grosvenor, A.P.; Kobe, B.A.; Biesinger, M.C.; McIntyre, N.S. Investigation of multiplet splitting of Fe 2p XPS spectra and bonding in iron compounds. *Surf. Interface Anal.* **2004**, *36*, 1564. [CrossRef]
75. Qi, F.; Peng, J.; Liang, Z.; Guo, J.; Liu, J.; Fang, T.; Mao, H. Strong metal-support interaction (SMSI) in environmental catalysis: Mechanisms, application, regulation strategies, and breakthroughs. *Environ. Sci. Ecotechnol.* **2024**, *22*, 100443. [CrossRef]
76. Magdziarz, A.; Colmenares, J.C.; Chernyayeva, O.; Lisovytskiy, D.; Grzonka, J.; Kurzydłowski, K.; Freindel, K.; Korecki, J. Insight into the synthesis procedure of Fe^{3+}/TiO_2-based photocatalyst applied in the selective photo-oxidation of benzyl alcohol under sun-imitating lamp. *Ultrason. Sonochem.* **2017**, *38*, 189–196. [CrossRef] [PubMed]
77. Kumar, M.R.A.; Abebe, B.; Nagaswarupa, H.P.; Murthy, H.C.A.; Ravikumar, C.R.; Sabir, F.K. Enhanced photocatalytic and electrochemical performance of TiO_2-Fe_2O_3 nanocomposite: Its applications in dye decolorization and as supercapacitors. *Sci. Rep.* **2020**, *10*, 1249. [CrossRef] [PubMed]
78. Aljuaid, J.; Timoumi, A.; Alamri, S.N. Investigation of the impact of iron amounts on optical and physical properties of coated TiO_2 thin films used for PV solar cells. *Optical Mater. X* **2022**, *16*, 100178. [CrossRef]
79. Kokorin, A.I.; Amal, R.; Teoh, W.Y.; Kulak, A.I. Studies of Nanosized Iron-Doped TiO_2 Photocatalysts by Spectroscopic Methods. *Appl. Magn. Reson.* **2017**, *48*, 447–459. [CrossRef]
80. Lian, J.; Duan, X.; Ma, J.; Peng, P.; Kim, T.; Zheng, W. Hematite (α-Fe_2O_3) with various morphologies: Ionic liquid-assisted synthesis, formation mechanism, and properties. *ACS Nano* **2009**, *3*, 3749–3761. [CrossRef]
81. Xie, M.; Deng, Q.; Yang, T.; Wang, C.; Liu, J.; Wen, F. One-step thermal oxidation synthesis of carbon-doped TiO_2 with enhanced photocatalytic activity using CO_2 as the carbon source. *J. Photochem. Photobiol. A Chem.* **2024**, *456*, 115822. [CrossRef]
82. Gao, H.; Ding, C.; Dai, D. Density functional characterization of C-doped anatase TiO_2 with different oxidation state. *J. Mol. Struct. THEOCHEM* **2010**, *944*, 156–162. [CrossRef]
83. Machado Garcia, R.; Carleer, R.; Arada Pérez, M.; Puente Torres, J.; Gu, Y.; Samyn, P.; Yperman, J. Fe-TiO_2/AC and Co-TiO_2/AC Composites: Novel Photocatalysts Prepared from Waste Streams for the Efficient Removal and Photocatalytic Degradation of Cibacron Yellow F-4G Dye. *Catalysts* **2021**, *11*, 1137. [CrossRef]
84. Thomas, M.; Naikoo, G.A.; Sheikh, M.U.D.; Bano, M.; Khan, F. Effective photocatalytic degradation of Congo red dye using alginate/carboxymethyl cellulose/TiO_2 nanocomposite hydrogel under direct sunlight irradiation. *J. Photochem. Photobiol. A Chem.* **2016**, *327*, 33–43. [CrossRef]
85. Shayegan, Z.; Haghighat, F.; Lee, C.-S. Carbon-doped TiO_2 film to enhance visible and UV light photocatalytic degradation of indoor environment volatile organic compounds. *J. Environ. Chem. Eng.* **2020**, *8*, 104162. [CrossRef]
86. Zhu, J.; Chen, F.; Zhang, J.; Chen, H.; Anpo, M. Fe^{3+}-TiO_2 photocatalysts prepared by combining sol–gel method with hydrothermal treatment and their characterization. *J. Photochem. Photobiol. A Chem.* **2006**, *180*, 196–204. [CrossRef]
87. Peacock, M.; Evans, C.D.; Fenner, N.; Freeman, C.; Gough, R.; Jones, T.G.; Lebron, I. UV-visible absorbance spectroscopy as a proxy for peatland dissolved organic carbon (DOC) quantity and quality: Considerations on wavelength and absorbance degradation. *Environ. Sci. Process. Impacts* **2014**, *16*, 1445–1461. [CrossRef] [PubMed]
88. Causse, J.; Thomas, O.; Jung, A.V.; Thomas, M.F. Direct DOC and nitrate determination in water using dual pathlength and second derivative UV spectrophotometry. *Water Res.* **2017**, *108*, 312–319. [CrossRef] [PubMed]
89. Jo, W.K.; Kumar, S.; Isaacs, M.A.; Lee, A.F.; Karthikeyan, S. Cobalt promoted TiO_2/GO for the photocatalytic degradation of oxytetracycline and Congo Red. *Appl. Catal. B Environ.* **2017**, *201*, 159–168. [CrossRef]
90. Bhaumik, M.; McCrindle, R.I.; Arjun Maity, A. Enhanced adsorptive degradation of Congo red in aqueous solutionsusing polyaniline/Fe^0 composite nanofibers. *Chem. Eng. J.* **2015**, *260*, 716–729. [CrossRef]
91. Shaban, M.; Abukhadra, M.R.; Ibrahim, S.S.; Shahien, M.G. Photocatalytic degradation and photo-Fenton oxidation of Congo red dye pollutants in water using natural chromite—Response surface optimization. *Appl. Water Sci.* **2017**, *7*, 4743–4756. [CrossRef]
92. Thanh, T.L.T.; Thi, L.N.; Dinh, T.T.; Van, N.N. Enhanced Photocatalytic Degradation of Rhodamine B Using C/Fe Co-Doped Titanium Dioxide Coated on Activated Carbon. *J. Chem.* **2019**, *2019*, 2949316. [CrossRef]
93. Zhang, J.; Kuang, M.; Wang, J.; Liu, R.; Xie, S.; Ji, Z. Fabrication of carbon quantum dots/TiO_2/Fe_2O_3 composites and enhancement of photocatalytic activity under visible light. *Chem. Phys. Lett.* **2019**, *730*, 391–398. [CrossRef]

94. Aboutaleb, W.A.; El-Salamony, R.A. Effect of Fe_2O_3-CeO_2 nanocomposite synthesis method on the Congo red dye photodegradation under visible light irradiation. *Mater. Chem. Phys.* **2019**, *236*, 121724. [CrossRef]
95. Mayoufi, A.; Nsib, M.F.; Houas, A. Doping level effect on visible-light irradiation W-doped TiO_2–anatase photocatalysts for Congo red photodegradation. *C. R. Chim.* **2014**, *17*, 818–823. [CrossRef]

Disclaimer/Publisher's Note: The statements, opinions and data contained in all publications are solely those of the individual author(s) and contributor(s) and not of MDPI and/or the editor(s). MDPI and/or the editor(s) disclaim responsibility for any injury to people or property resulting from any ideas, methods, instructions or products referred to in the content.